Influence of fault geometries and mechanical anisotropies on the growth and inversion of hanging-wall synclinal basins: insights from sandbox models and natural examples

O. FERRER[1,2]*, K. McCLAY[1] & N. C. SELLIER[1]

[1]*Fault Dynamics Research Group, Department of Earth Sciences, Royal Holloway University of London, Egham, Surrey TW20 0EX, UK*

[2]*Geomodels Research Institute, Departament de Geodinàmica i Geofísica, Facultat de Geologia, Universitat de Barcelona, C/Martí i Franquès s/n, 08028 Barcelona, Spain*

Corresponding author (e-mail: joferrer@ub.edu)

Abstract: Salt is mechanically weaker than other sedimentary rocks in rift basins. It commonly acts as a strain localizer, and decouples supra- and sub-salt deformation. In the rift basins discussed in this paper, sub-salt faults commonly form wide and deep ramp synclines controlled by the thickness and strength of the overlying salt section, as well as by the shapes of the extensional faults, and the magnitudes and slip rates along the faults. Upon inversion of these rift basins, the inherited extensional architectures, and particularly the continuity of the salt section, significantly controls the later contractional deformation.

This paper utilizes scaled sandbox models to analyse the interplay between sub-salt structures and supra-salt units during both extension and inversion. Series 1 experiments involved baseline models run using isotropic sand packs for simple and ramp-flat listric faults, as well as for simple planar and kinked planar faults. Series 2 experiments involved the same fault geometries but also included a pre-extension polymer layer to simulate salt in the stratigraphy. In these experiments, the polymer layer decoupled the extensional and contractional strains, and inhibited the upwards propagation of sub-polymer faults. In all Series 2 experiments, the extension produced a synclinal hanging-wall basin above the polymer layer as a result of polymer migration during the deformation. During inversion, the supra-polymer synclinal basin was uplifted, folded and detached above the polymer layer. Changes in thickness of the polymer layer during the inversion produced primary welds and these permitted the sub-polymer deformation to propagate upwards into the supra-salt layers.

The experimental results are compared with examples from the Parentis Basin (Bay of Biscay), the Broad Fourteens Basin (southern North Sea), the Feda Graben (central North Sea) and the Cameros Basin (Iberian Range, Spain).

Salt strata within rift basins commonly localizes strains and decouples sub- and supra-salt deformation because it is mechanically significantly weaker than other units (e.g. Jackson & Vendeville 1994; Letouzey *et al.* 1995; Nalpas *et al.* 1995; Withjack & Callaway 2000; Dooley *et al.* 2005; Krzywiec 2006). As a result of this strength contrast, the style of supra- and sub-salt deformation can be significantly different. In a rift system without salt layers, the basement extension is accommodated by the upwards propagation of faults throughout the syn-extensional basin fill (i.e. thick-skinned extension) (Ellis & McClay 1988; McClay 1989; Withjack & Callaway 2000; Corti 2012) (Fig. 1a, c). In contrast, in rift systems with salt layers, the basement extension triggers salt flow towards the margins of the basin decoupling the deformation of sub- and supra-salt units and inhibits the upwards propagation of the sub-salt faults, which results in decoupled thin-skinned extension in the supra-salt layers (Nalpas & Brun 1993; Jackson & Vendeville 1994; Soto *et al.* 2007; Ferrer *et al.* 2008*a*, *b*, 2014). Similarly, upon inversion of rift basins without salt in the stratigraphic section, the inverted fault systems propagate upwards from the rift strata into the overlying post-rift and syn-inversion strata (Fig. 1b, d) (e.g. McClay 1989; Buchanan & McClay 1992; McClay & Buchanan 1992).

Factors that control coupled/decoupled deformation and the geometries of the supra-salt section include:

- the thicknesses and strength of the salt layer and the overburden layers;

From: Childs, C., Holdsworth, R. E., Jackson, C. A.-L., Manzocchi, T., Walsh, J. J. & Yielding, G. (eds) *The Geometry and Growth of Normal Faults*. Geological Society, London, Special Publications, **439**, http://doi.org/10.1144/SP439.8

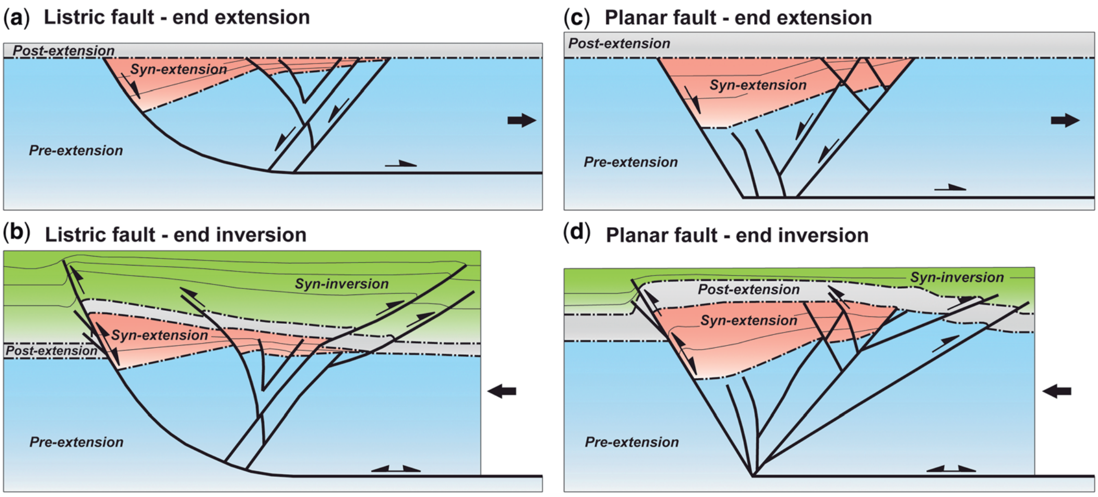

Colour online/ mono hardcopy

Fig. 1. Synoptic models for extension and inversion of (**a**) & (**b**) a simple listric fault and (**c**) & (**d**) a simple planar fault dipping 60° (modified from McClay 1995).

- the geometry of the main extensional fault;
- the rate of fault slip;
- the magnitude of displacement on the basin-bounding fault;
- the location of the salt strata within the basin stratigraphy (i.e. pre-, syn- or post-kinematic) (e.g. Jackson *et al.* 1990; Koyi *et al.* 1993; Jackson & Vendeville 1994; Withjack & Callaway 2000; Soto *et al.* 2007; Ferrer *et al.* 2008*b*, 2014).

During extension, a thin salt layer or a very fast slip rate on the main bounding fault will prevent salt flow and produce coupled deformation between the supra- and sub-salt strata (i.e. sub-salt structures will propagate upwards through the stratigraphic section). In contrast, a thick salt layer or a slow fault slip rate favours salt flow and the development of a hanging-wall monocline or synclinal basin above the major extensional fault (e.g. Withjack & Callaway 2000). In this case, salt acts as an intermediate extensional décollement absorbing deformation and inhibiting fault propagation from the sub-salt units through to the supra-salt layers. Similarly, evaporite compositions and strengths may also control the deformation of the supra-evaporite units decoupling supra- and sub-salt layers. Wet halite has an extremely low shear strength at geological strain rates (e.g. Vendeville & Jackson 1992) in comparison with gypsum or anhydrite. Halite preferably deforms very easily and flows acting as a regional detachment surface (e.g. Fiduk & Rowan 2012; Butler *et al.* 2014; Dooley *et al.* 2015). In addition, changes in the salt thickness related to the original salt syn-depositional environment (pre-, syn- or post-rift) may also control the degree of decoupling during extension (e.g. Jackson & Vendeville 1994; Coward & Stewart 1995; Ferrer *et al.* 2008*b*, 2014).

Many rift basins containing salt strata have also undergone later contractional deformation (inversion) where the main normal faults have been reactivated, producing contractional geometries superposed on the pre-existing extensional rift architectures. Where there is no salt section in the rift basin system, the main faults may propagate upwards during inversion without decoupling, and produce asymmetric anticlines, harpoon structures and hanging-wall back-thrusts as a result of buttressing or footwall shortcut faults (McClay 1989, 1995; Bonini *et al.* 2012) (Fig. 1b, d). In contrast, in rift basins with salt units, the salt structures at the end of extension will critically control the kinematics and geometries of the inverted salt basins producing partial or fully decoupled contractional deformation. Primary salt welds as a result of salt depletion during extension will inhibit later salt migration and the development of detachment folds during inversion. Natural examples of inverted salt basins with similar structural features to those described above include the central and southern North Sea (Van Wijhe 1987; Gowers *et al.* 1993; Nalpas *et al.* 1995), the Mid-Polish Trough with Zechstein evaporites (Krzywiec 2006; Burliga *et al.* 2012; Rowan & Krzywiec 2014), the Pyrenean rift basins (García-Senz 2002; Ferrer *et al.* 2008*a*, 2012; Roca *et al.* 2011), and the Atlas Mountains (Letouzey *et al.* 1995; Teixell *et al.* 2003).

Scaled physical models are a widely used, powerful tool for studying the geometry and kinematics of basin structures formed during both extension (e.g. McClay 1990; Corti 2012) and inversion (e.g. review by Bonini *et al.* 2012). Many previously

Table 1. *Experimental models described in this paper*

Fault geometry	Series 1 baseline isotropic models without polymer	Series 2 anisotropic models with polymer
Simple listric	Exp. 1.1	Exp. 2.1
Ramp-flat listric	Exp. 1.2	Exp. 2.2
Simple planar (20°)	Exp. 1.3	Exp. 2.3
Simple planar (60°)	Exp. 1.4	Exp. 2.4
Kinked planar (60° and 20°)	Exp. 1.5	Exp. 2.5

published sandbox models of inverted fault systems with a rigid fault footwall did not include significant mechanical anisotropies in the sand packs (i.e. ductile polymer layers) within the hanging-wall stratigraphy (e.g. McClay 1989, 1995; Buchanan & McClay 1991; Keller & McClay 1995) (Fig. 1). Only the experiments of Soto *et al.* (2007) and Ferrer *et al.* (2008*b*, 2014) included a weak layer (pre- or syn-kinematic) and a rigid footwall fault during extension. However, the inversion of basins with mechanical anisotropies has been modelled using other sandbox configurations or numerical models (e.g. Nalpas *et al.* 1995; Brun & Nalpas 1996; Dubois *et al.* 2002; Panien *et al.* 2005, 2006; Del Ventisette *et al.* 2006; Buiter *et al.* 2009; Bonini *et al.* 2012; Burliga *et al.* 2012). Many of these experiments used a basal plastic sheet or a metal plate attached to the moving wall to produce the extension and the inversion to the brittle–ductile layers in the hanging wall. The review of Bonini *et al.* (2012) showed that in brittle–ductile models the geometry of the fault is imposed by the velocity discontinuity between the basal mobile plate and the fixed part of the experiment, whereas models with rigid footwall blocks permit the simulation of hanging-wall geometries above a variety of footwall fault geometries (e.g. Fig. 1). However, fixed footwall fault models do not allow the deformation of the rigid footwall with subsequent development of footwall shortcut thrusts during inversion.

Taking the above limitation into account, this paper presents two series of extension–inversion sandbox models with rigid footwall blocks. Series 1 experiments were isotropic sandbox models, whereas Series 2 models contained a pre-kinematic polymer layer that simulated a salt section in the natural prototypes (Table 1). The experimental results are compared with published natural examples of inverted extensional basins that contain evaporite units.

Research methodology

Experimental set-up

The experimental set-up used was similar to that applied by Yamada & McClay (2003*a*, *b*, 2004). Sandbox experiments were carried out in a glass-sided deformation rig that was 150 cm long, 30 cm wide and up to 20 cm deep (Fig. 2). An electric motor fixed to the base plate drove a worm screw attached to the footwall block that produced uniaxial lengthening or shortening and normal or reverse slip of the basement fault. A constant displacement rate of 1.83×10^{-4} cm s^{-1} was applied in all the experiments during both extension and inversion in order to allow ductile flow of the polymer layers in Series 2 experiments. A strong flexible plastic sheet (but not deformable under the model conditions) was used as a detachment surface between the rigid footwall and the hanging-wall sand pack. This sheet was attached to the fixed end walls of the apparatus, maintaining constant length during the experiments. The weight of the hanging-wall sand forced the plastic sheet to conform to the underlying footwall fault block (Fig. 2). This experimental configuration allowed sliding of the plastic sheet without any length changes above the footwall surface during extension and inversion (i.e. Yamada & McClay 2003*a*, *b*, 2004). The coefficient of sliding friction between the plastic detachment and the sand pack was $\mu_b = 0.37$ (Huiqi *et al.* 1992). The main limitation of this experimental set-up using a rigid footwall is that it does not allow footwall deformation during inversion, such as occurs in natural analogues (e.g. McClay 1989, 1995; Buchanan & McClay 1991; Bonini *et al.* 2012). Keeping the above limitations in mind, five different footwall fault geometries were used in the experimental programme presented in this paper (Table 1):

(1) concave-upwards simple listric fault;
(2) ramp-flat listric fault;
(3) simple planar fault dipping 20°;
(4) simple planar fault dipping 60°;
(5) kinked planar fault with an upper 60° dipping panel and a lower panel that dips 20° onto the flat basal detachment.

The hanging-wall sand pack consisted of layered moderately well-rounded and well-sorted coloured and uncoloured dry quartz sand, with an average grain size of 0.25 mm, that was used to simulate

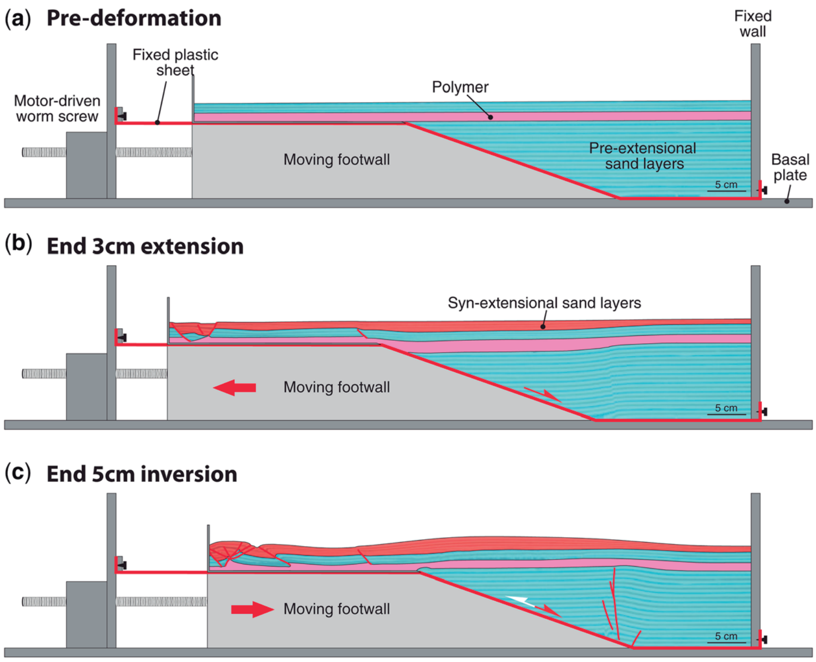

Fig. 2. Experimental set-up and sedimentary infill for each deformational episode: (**a**) pre-deformation geometry; (**b**) configuration of the experiment at the end of the extension; and (**c**) experimental configuration at the end of the inversion.

Colour online/ mono hardcopy

brittle sedimentary rocks in the upper crust. The sand was washed and dyed using blue, red, black or yellow pigments, and then oven-dried for 12 h at 100°C. In order to ensure that the mechanical behaviour of the uncoloured sand was similar to that of the dyed coloured sand, uncoloured sand was washed to remove the fine fraction (<20 μm) and then also oven-dried at 100°C for 12 h.

The layered sand pack was constructed by pouring alternating layers of sand into the deformation apparatus and then levelled using a mechanical scraper (e.g. Krantz 1991; Lohrmann *et al.* 2003). Figure 2a shows the pre-kinematic hanging-wall strata formed by alternating 2.5 mm layers of blue, black and white sand, with a total thickness of 10 cm. In Series 2 experiments (Fig. 2a), a uniform 12 mm-thick polymer layer was extended across the whole model and onto the footwall block. The polymer is a long-chain polydimethylsiloxane (PDMS) that deforms by viscous flow and is widely used as analogue for the natural deformation of salt at geological strain rates (Weijermars 1986). Finally, the polymer layer was overlaid with pre-extensional strata formed by alternating 2.5 mm layers of blue, white and black sand up to a thickness of 1.5 cm (Fig. 2a).

The mechanical properties of the poured sand were measured using a ring shear tester at the Fault Dynamics Research Group laboratory. The poured dry quartz sand used in these experiments has an angle of internal friction of 34.6°, a bulk density of 1500 kg m^{-3}, a coefficient of internal friction of 0.69 and a low apparent cohesive strength of 55 Pa. It deforms according to Navier–Coulomb failure at moderate and high values of normal stress (i.e. Horsfield 1977; McClay 1990). The PDMS used in the experimental programme (Rhodia Rhodosil Gum FB) is a near-perfect Newtonian fluid with a density of 0.972 g cm^{-3} at room temperature and a viscosity of 1.6×10^4 Pa s when deformed at a laboratory strain rate of 1.83×10^{-4} cm s^{-1} (Dell'Ertole & Schellart 2013). The main properties of the analogue materials and their scaling parameters used in the experimental programme are summarized in Table 2, and Figure 3 shows the general strength profiles for the analogue models described in this paper.

Experimental procedure

All models underwent 3 cm of total extension during which syn-extensional layers of red, white and black sand were added episodically after every 5 mm of extension (Fig. 2b). The regional level for each syn-kinematic layer was increased by 1 mm for every 5 mm of extension in order to preserve structures formed by polymer inflation. After the extension, models were then shortened

Table 2. *Scaling parameters used in the experimental programme*

Quantity	Experiment	Nature	Model ratio
Thickness			
Overburden	21–45 mm	2–4 km	1.05×10^{-5}–1.125×10^{-5}
Salt/polymer	12 mm	1000 m	1.2×10^{-5}
Density			
Overburden	1500 kg m^{-3}	2700 kg m^{-3}	0.55
Salt/polymer	972 kg m^{-3}	2200 kg m^{-3}	0.44
Density contrast	528	500	1.05
Ductile layer viscosity	1.6×10^{-4} Pa s	10^{-18}–10^{-19} Pa s	1.6×10^{-14}–1.6×10^{-15} Pa s
Overburden coefficient friction	0.7	0.8	0.87
Gravity acceleration	9.81 m s^{-2}	9.81 m s^{-2}	1

5 cm (Fig. 2c). The amount of shortening was higher than the applied extension to force the polymer to act as a contractional detachment, transferring part of the deformation into the footwall of the rigid fault block. No syn-contractional strata were deposited during the inversion (Fig. 2c). At the end of each experiment, the models were preserved and sliced in closely spaced vertical serial sections (3 mm thick) in order to analyse the internal fault geometries. A 5 cm-wide section along each side-wall of the models was discarded in order to eliminate edge effects produced by friction between the sand pack and the glass sidewalls.

Analysis of the analogue models

High-resolution time-lapse photographs of the upper part of the models and the sidewalls were taken every 2 min by computer-controlled digital cameras in order to record the kinematic evolution of the experiments.

The pictures of the vertical cross-sections through the physical models were studied using image-processing software in order to produce 3D voxel models for analysing cross-sections and depth slices.

Analogue model results

In this section, the results of the Series 1 and Series 2 experiments (Table 1) are described. In each case, the results of sandbox models with and without a pre-kinematic polymer layer are compared first for extension and then for inversion. All models were subjected to dip-slip extension, followed by dip-slip inversion. There was no strike-slip deformation and

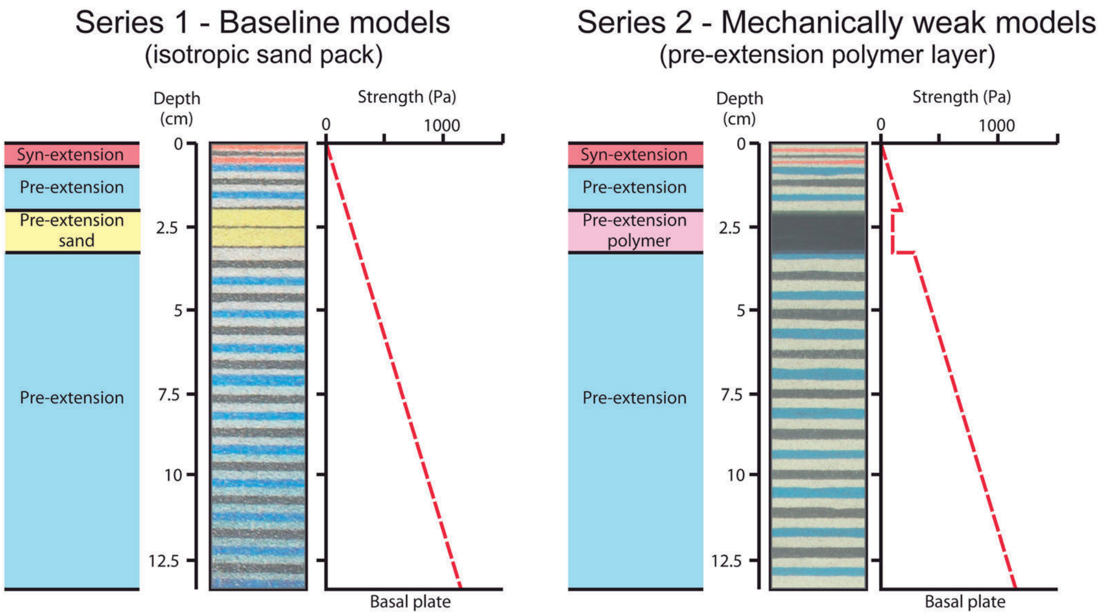

Colour online/mono hardcopy

Fig. 3. Hanging-wall sand pack configurations and schematic strength profiles for the experimental programme.

only minor oblique slip on some small faults due to 3D space issues associated with local complex inversion geometries.

Extension above listric fault systems

Simple listric and ramp-flat listric faults without a pre-kinematic polymer layer. The geometrical hanging-wall evolution of models with an isotropic sand pack above a simple listric fault and a ramp-flat listric fault (Series 1 – baseline models) are shown in Figure 4a, b. These are similar to previously published models in McClay & Ellis (1987*a*, *b*), Ellis & McClay (1988), McClay (1989), Buchanan & McClay (1991), McClay & Scott (1991), McClay *et al.* (1991), Soto *et al.* (2007) and Ferrer *et al.* (2014).

Whereas a simple hanging-wall rollover developed in the simple 45° listric model (Fig. 4a), the deformation above a 60° ramp-flat listric fault

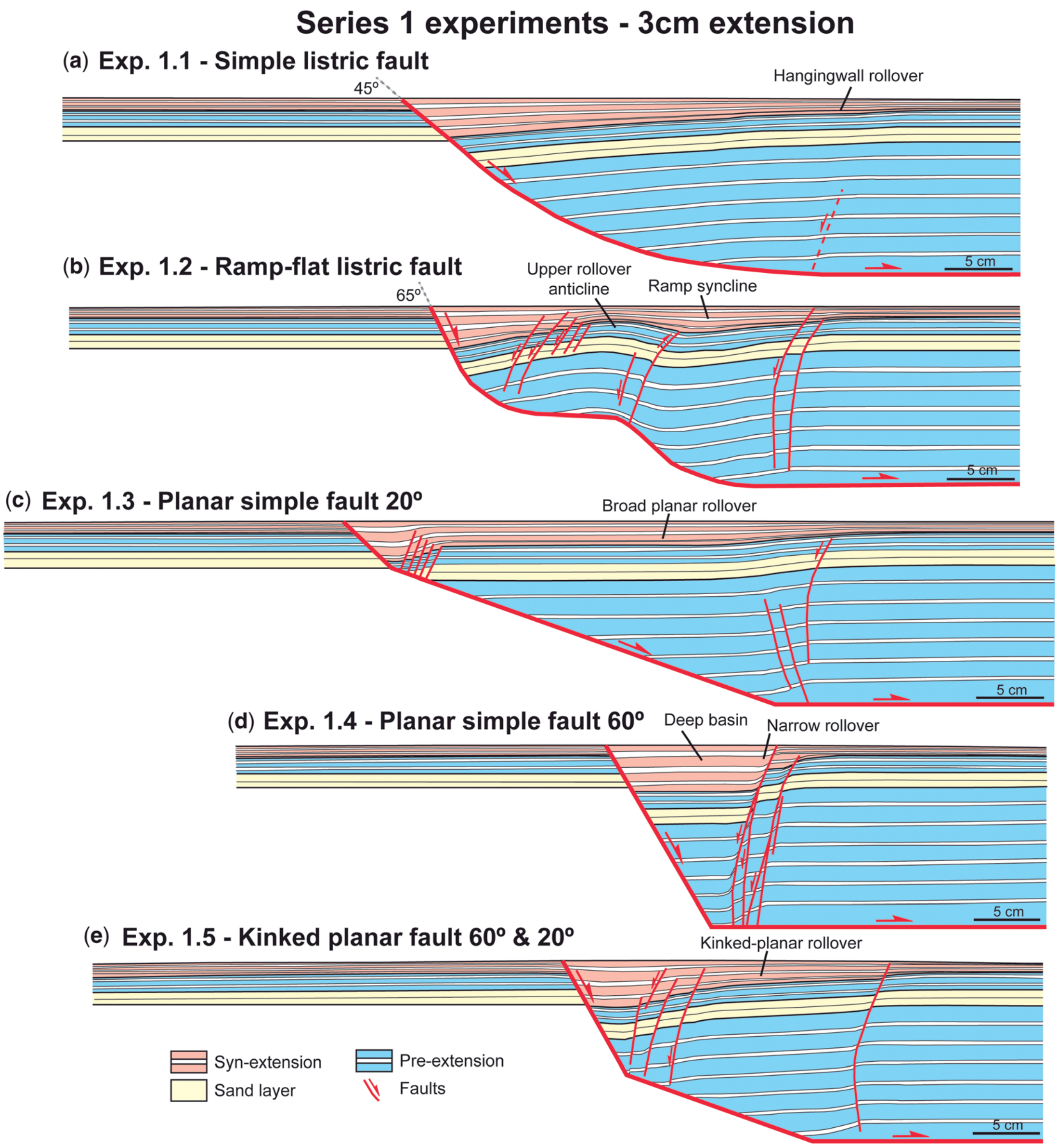

Colour online/colour hardcopy

Fig. 4. Model cross-sections illustrating the structural style after 3 cm of extension for the Series 1 baseline isotropic experiments without a pre-kinematic polymer layer: (**a**) simple 45° listric fault; (**b**) ramp-flat 60° listric fault; (**c**) simple planar fault dipping 20°; (**d**) simple planar fault dipping 60°; and (**e**) kinked planar fault with two panels dipping 60° and 20°. Yellow sand layers are in an equivalent position to the polymer layers in Figure 5.

produced a rollover anticline associated with the upper 60° listric fault segment, an adjacent ramp syncline formed above the convex upwards ramp section and a lower rollover associated with the lower listric fault segment (Fig. 4b). In the simple 45° listric fault model, only minor antithetic faulting developed due to the large radius of curvature of the listric part of the fault surface (Fig. 4a). Only minor antithetic faults developed in the hanging wall of the 60° ramp-flat listric fault (Fig. 4b). Similarly, the small amount of extensional displacement in both the listric and the ramp-flat listric faults did not develop sufficient internal strains to form crestal-collapse graben in the rollover anticlines (Fig. 4a, b). In these Series 1 listric fault models, the minor antithetic faults and the main basin-bounding fault propagated across the entire sand pack. Hanging-wall growth strata in the simple 45° listric fault formed a simple fanning wedge (Fig. 4a): in the 60° ramp-flat listric fault, however, the upper rollover formed a fanning growth wedge, but the ramp syncline and lower rollover combined to form a gentle synclinal wedge (Fig. 4b).

Simple listric and ramp-flat listric faults with a pre-kinematic polymer layer. The listric fault models with a pre-kinematic polymer layer formed supra-salt hanging-wall synclinal basins that were coupled from the underlying faulted, sub-salt strata (Fig. 5a, b). The evolution of the strata below the pre-kinematic polymer layer was similar to that described above (e.g. Fig. 4a, b). In the simple 45° listric model, however, decoupling by the polymer layer, together with polymer flow, produced a broad hanging-wall monocline in the sand pack above the polymer above the fault breakaway (Fig. 5a). A gentle extensional fault-propagation fold developed as the extension progressed, with syn-kinematic layers enlarging the resultant synclinal basin. The subsidence of the basin depocentre, combined with the hanging-wall extension, induced polymer migration towards the rollover hinge as well as above the rigid footwall to form a gentle broad polymer-cored anticline (Fig. 5a). No faulting occurred in the supra-salt section.

In the 60° ramp-flat listric model, the supra-polymer decoupling was more pronounced, with a main synclinal depocentre formed by the upper rollover, together with a polymer-cored anticline over the ramp section of the basin-bounding fault and secondary depocentre formed by the lower rollover (Fig. 5b). Polymer migration is clearly evident from the thickened section in the immediate hanging wall of the upper 60° listric fault segment, as well as in the ramp syncline. As in the simple 45° listric fault model described previously (Fig. 5a), in the 60° ramp-flat model no primary welds were formed nor was there any development of new faults in the supra-salt sand pack owing to the small amount (3 cm) of extension (Fig. 5b).

In addition to the main synclinal basins, narrow distal footwall supra-polymer graben developed near footwall extremities of the polymer layer in both listric fault models (Fig. 5a, b). These were probably produced by a boundary effect at the edge of the polymer detachment (cf. Vendeville & Jackson 1992; Jackson & Vendeville 1994). These graben were infilled by syn-kinematic sand layers as extension progressed, and this suppressed the formation of polymer walls and diapirs at this location (e.g. Vendeville & Jackson 1992).

Extension above planar fault systems

Simple planar and kinked planar faults without a pre-kinematic polymer layer. The sandbox models with planar footwall detachment faults are characterized by planar or gently kinked rollover anticlines (Fig. 4c–e). The hanging-wall architectures are similar to those in models published by McClay & Ellis (1987*a*, *b*), Ellis & McClay (1988), McClay *et al.* (1991), Withjack *et al.* (1995), Dooley *et al.* (2005), Withjack & Schlische (2006) and Ferrer *et al.* (2014). The hanging-wall rollover geometries were controlled by the amount of extension (3 cm), by the dips of the bounding faults (Fig. 4c, d) and by the kink-band bend in the fault surface for Series 1 Model 1.5 (Fig. 4e). In the models described in this paper, the hanging-wall faults are dominantly antithetic (Fig. 4c–e). The 20° planar fault model formed a broad planar rollover with localized, small antithetic faults near the detachment breakaway (Fig. 4c). The 60° dipping planar bounding fault model produced a narrow rollover with closely spaced antithetic faults that bound a deep, flat half-graben basin (Fig. 4d). The 60°–20° kinked planar fault model formed a broad, gently kinked, hanging-wall fault-bend fold (Fig. 4e). Similar to the listric fault models described above, these planar fault models showed no internal decoupling, with the antithetic faults cutting from the syn-kinematic into the pre-kinematic sand layers (Fig. 4c–e).

Simple planar and kinked planar faults with a pre-kinematic polymer layer. In contrast to the experimental results discussed above, the models of planar faults containing a pre-kinematic polymer layer formed hanging-wall structures where the supra-salt deformation was decoupled from the underlying sub-salt deformation (Fig. 5c–e). The resultant hanging-wall basins are synclinal depocentres infilled with syn-kinematic growth stratal wedges. The dip of the basin-bounding fault controlled the form of the synclines, whereby the 20° planar fault model formed a broad synclinal basin (Fig. 5c), and the more steeply dipping 60° planar fault models formed deeper and narrow synclines (Fig. 5d, e). The sub-polymer deformation was characterized by antithetic faults that could not link upwards through the polymer layer into the supra-salt section.

The progressive evolution of Series 2 Model 2.4, a 60° dipping planar fault, is shown in detail in Figure 6. After 1 cm of extension, the sub-salt section had formed a narrow, flat hanging-wall graben bounded by a narrow rollover with very steep, planar antithetic faults (Fig. 6b). Above the polymer layer, a broad syncline had formed. At this stage of the extension, faulting underneath the polymer layer created accommodation space that triggered polymer flow into the depocentre from the footwalls of the basin-bounding faults (Fig. 6b). As extension progressed, the deformation was decoupled by the polymer layer, with brittle extensional faults in the sub-polymer units and a broad growth syncline in the supra-polymer strata (Fig. 6c, d). In this 60°

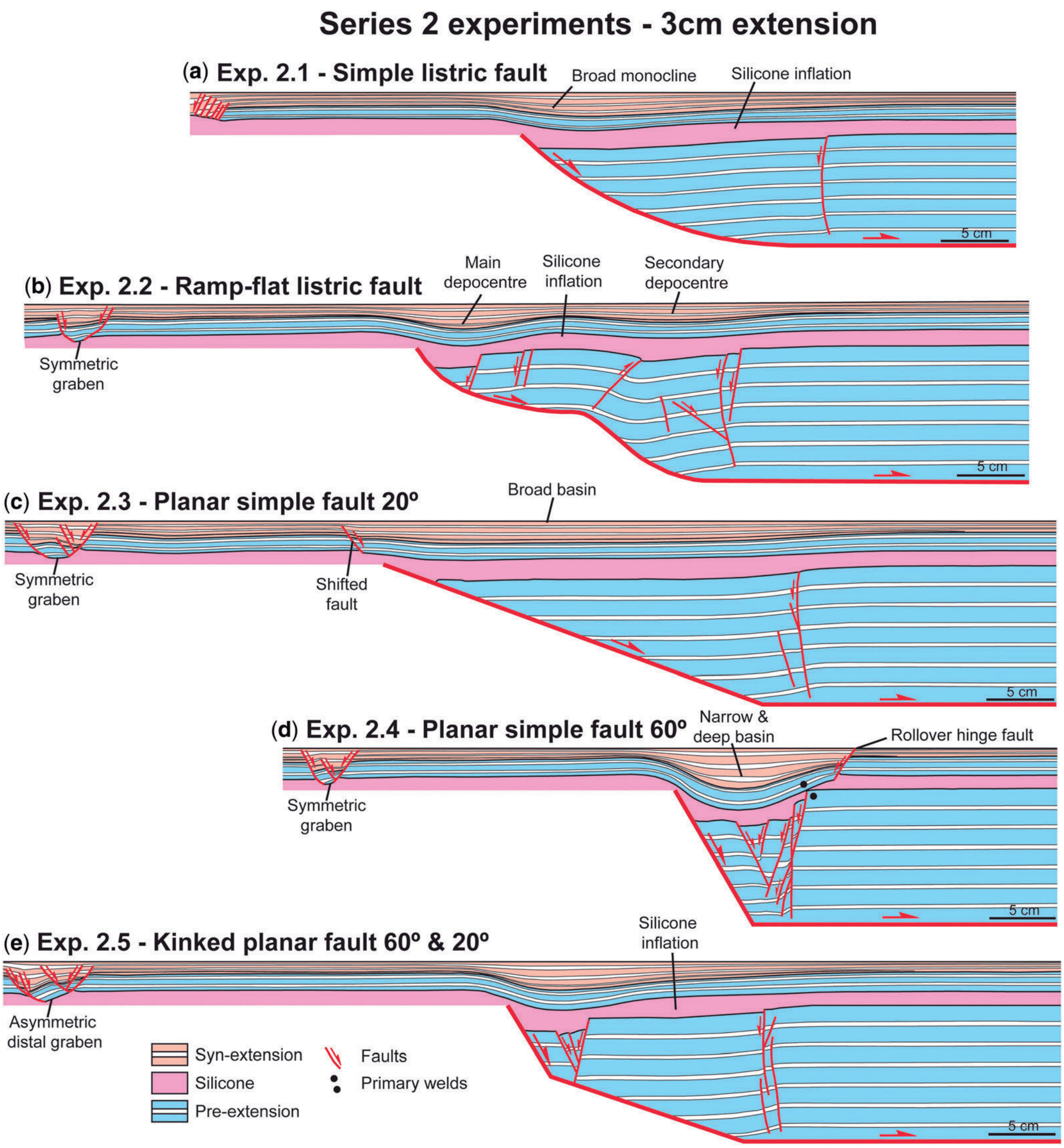

Colour online/ colour hardcopy

Fig. 5. Model cross-sections illustrating the structural style after 3 cm of extension for the Series 2 anisotropic experiments with a pre-kinematic polymer layer: (**a**) simple 45° listric fault; (**b**) ramp-flat 60° listric fault; (**c**) simple planar fault dipping 20°; (**d**) simple planar fault dipping 60°; and (**e**) kinked planar fault with two panels dipping 60° and 20°. The polymer layers are in an equivalent position to the yellow sand layers in Figure 4.

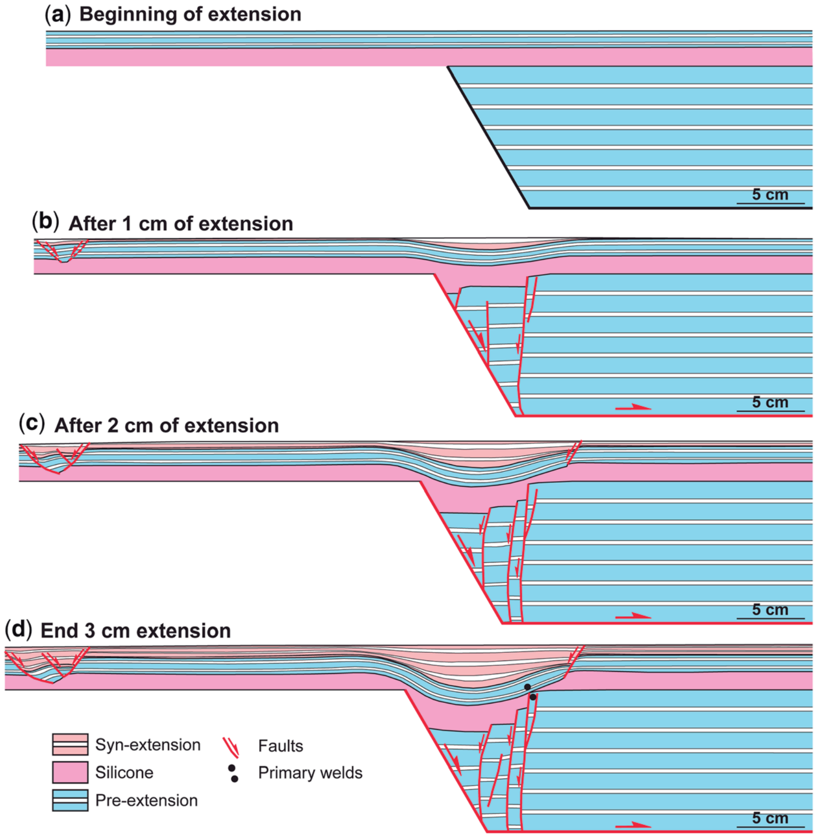

Fig. 6. Extensional evolution of the 60° planar fault model: (**a**) initial set-up – 0 cm of extension; (**b**) after 1 cm of extension; (**c**) after 2 cm of extension; and (**d**) at the end of 3 cm of extension.

Colour online/ mono hardcopy

planar fault model, primary weld formed over the footwall of the main rollover antithetic fault (Fig. 5c, d). A few small displacement extensional faults developed in the strata above the polymer layer (Fig. 5c, d).

In addition to the main synclinal basins, narrow distal footwall supra-polymer graben developed near footwall extremities of the polymer layer in models with planar faults (Figs 5c–e & 6). As described in the subsection on 'Extension above listric fault systems', these narrow graben are related to the edge effects where the polymer layer ends.

Inversion

In terms of classification of inverted basins by Bally (1984), the analogue models described in this paper were at the early stages of net compressional tectonics, where the 5 cm of contractional reactivation was greater than the 3 cm of previous extension (Figs 7–9). All of the models show the reactivation of the major basin-bounding fault during inversion. Inversion of Series 1 models without a ductile polymer layer produced reactivation and basin uplift, with the formation of harpoon structures (e.g. Fig. 7). Inversion of Series 2 models with a pre-extension ductile polymer layer produced mainly decoupling between the layers above the polymer and the layers below (e.g. Fig. 8). In these models, the inversion arched and uplifted the synclinal basins, and reduced the thickness of the ductile layer, which eventually hindered the flow of the polymer. In some models, where the polymer layer was totally depleted, the formation of primary welds dramatically controlled the final inversion geometry. The welds inhibited detachment on the polymer layer and allowed uplift of the underlying pre-kinematic units (Fig. 8).

Inversion of listric extensional fault systems

Inversion of listric faults without a pre-extension polymer layer. The inversion geometries of the Series 1 baseline listric fault models were similar to those described in the papers of Buchanan & McClay (1991), McClay & Buchanan (1992), Keller & McClay (1995) or McClay (1995) (Fig. 7a, b).

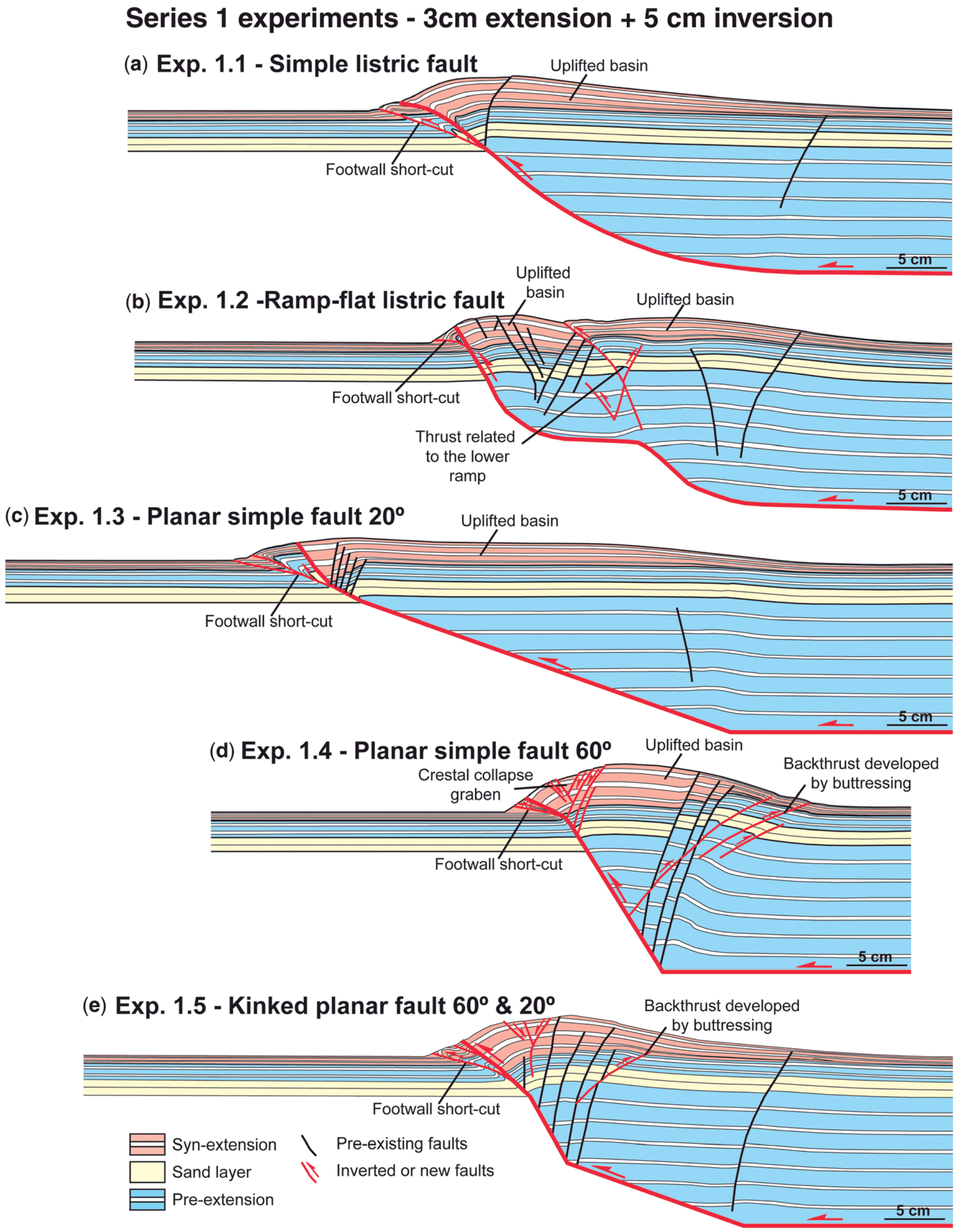

Colour online/colour hardcopy

Fig. 7. Model cross-sections illustrating the structural style after 5 cm of inversion for the Series 1 baseline isotropic experiments without a pre-kinematic polymer layer: (**a**) simple 45° listric fault; (**b**) ramp-flat 60° listric fault; (**c**) simple planar fault dipping 20°; (**d**) simple planar fault dipping 60°; and (**e**) kinked planar fault with two panels dipping 60° and 20°.

Inversion of the 45° simple listric fault reactivated the major detachment fault, producing reverse slip together with uplift and back-rotation of the hanging wall (Fig. 7a). Owing to the low dip of the listric fault, the amount of back-rotation is low and a simple harpoon structure was formed with a

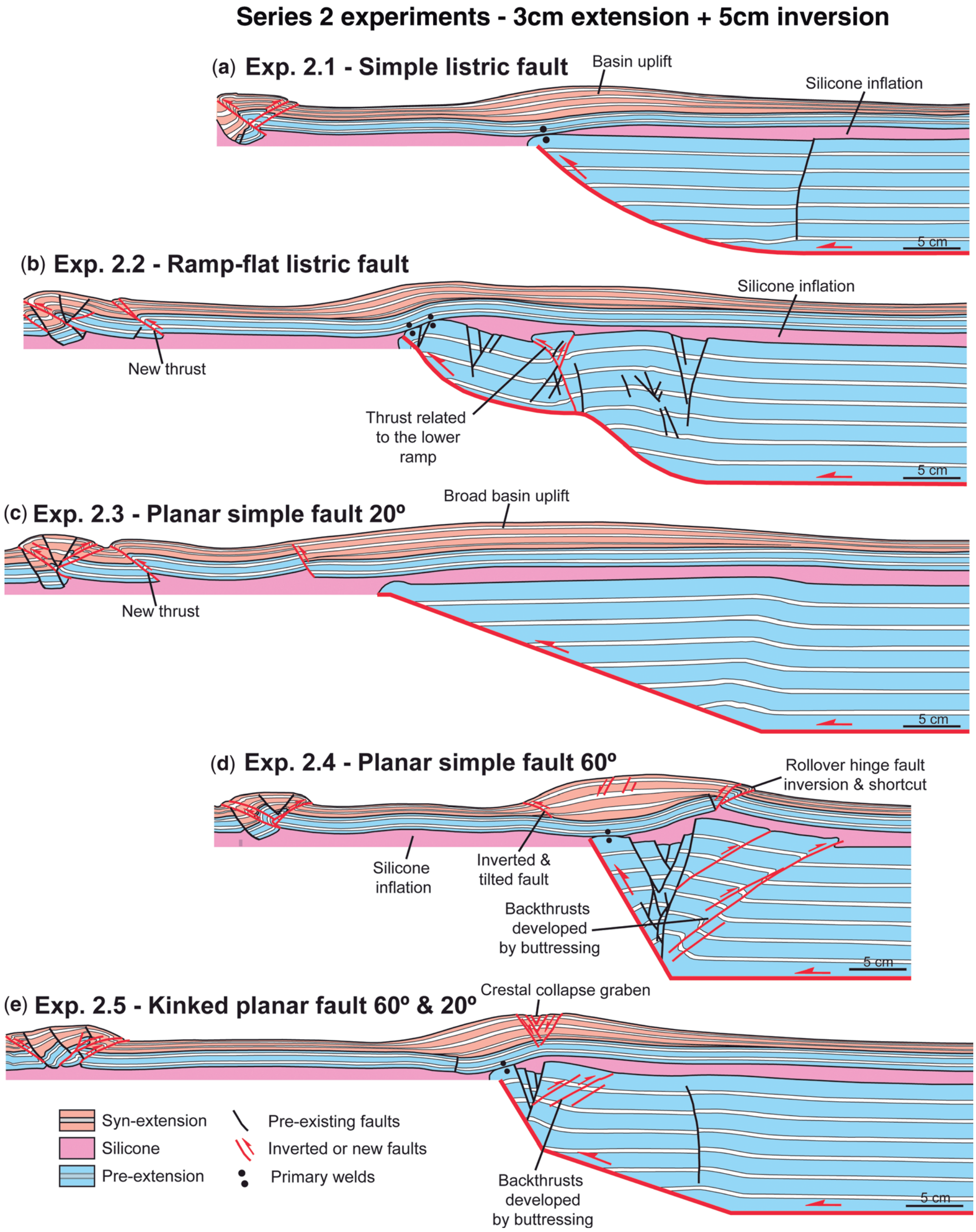

Colour online/ colour hardcopy

Fig. 8. Model cross-sections illustrating the structural style after 5 cm of inversion for the Series 2 anisotropic experiments with a pre-kinematic polymer layer: (**a**) simple 45° listric fault; (**b**) ramp-flat 60° listric fault; (**c**) simple planar fault dipping 20°; (**d**) simple planar fault dipping 60°; and (**e**) kinked planar fault with two panels dipping 60° and 20°.

low-angle footwall shortcut thrust into the footwall stratigraphy (Fig. 7a). The low-amplitude asymmetrical inversion anticline has a front-limb dip of approximately 28° and very gentle back-limb dip of 4°. The model is in net contraction, with the syn-kinematic layers uplifted above regional.

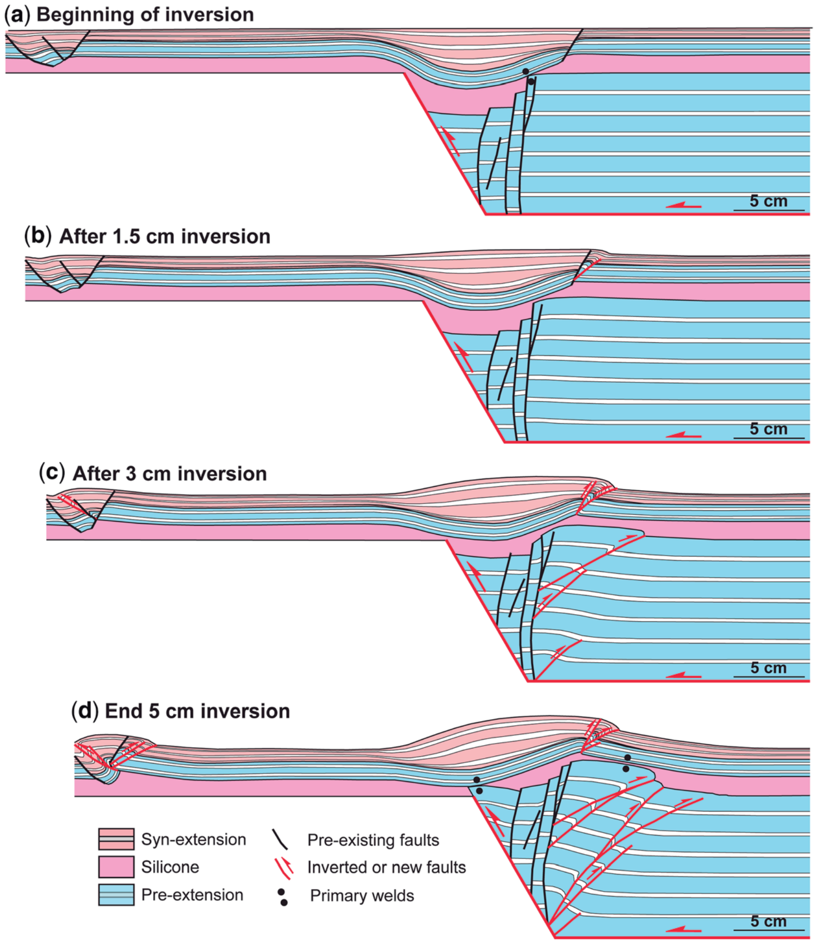

Colour online/ mono hardcopy

Fig. 9. Evolution of the 60°-dipping planar fault model during the inversion: (**a**) cross-section at the end of 3 cm of extension – 0 cm of inversion; (**b**) after 1.5 cm of shortening; (**c**) after 3 cm of shortening – total inversion; and (**d**) at the end of 5 cm of inversion – net contraction.

Inversion of the 60° ramp-flat listric fault model reactivated the main detachment and uplifted the hanging-wall basin onto the footwall strata (Fig. 7b). A frontal asymmetric anticline formed above the breakaway of the main detachment fault, with a front-limb dip of 35° and a gentle back-limb dip of 6–7° (Fig. 7b). A footwall shortcut thrust developed in the footwall strata in front of the inverted basin. A footwall-vergent, hanging-wall bypass thrust formed along the trajectory of the ramp section of the main detachment and propagated upwards, thrusting the extensional ramp syncline over the inverted rollover anticline (Fig. 7b). In both Series 1 listric models, inversion of the main detachment fault produced uplift and the arching of the synclinal syn-extensional basins.

Inversion of listric faults with a pre-extension polymer layer. The inversion of Series 2 listric fault models that contain a pre-extensional polymer layer produced almost completely decoupled deformation (Fig. 8a, b).

In the simple 45° listric fault model with the pre-extensional polymer layer, the 5 cm of contraction reactivated the main detachment and fully inverted the sub-polymer pre-extension strata, producing a broad uplift of the supra-polymer and syn-extension hanging-wall basin (Fig. 8a). A primary polymer weld formed at the crest of the very gentle inversion anticline where the polymer thinned by flow towards both the footwall and hanging wall. The small ‘end effect’ graben on the footwall block at the extremities of the polymer layer was inverted and uplifted by small bi-vergent thrust faults (Fig. 8a). In this model, the asymmetrical inversion anticline is only very small due partly to the low angle of the reactivated detachment and due also to the decoupling of the polymer, which transfers the shortening into broad folding and uplift of the syn-extensional strata above their regional, as well as thrusting at the footwall extremities of the polymer layer (Fig. 8a).

Inversion of the 60° ramp-flat listric fault produced a similar overall decoupled architecture to the simple listric fault described above but with a larger asymmetric frontal inversion anticline, and a greater and broader uplift of the syn-extensional strata above their regional level (Fig. 8b). The polymer layer underwent significant internal flow with thinning and weld formation at the crest of the frontal inversion anticline, as well as thickening and inflation in the hanging wall and at the distal extremity of the footwall (Fig. 8b). The upper sub-polymer pre-extension strata in the hanging-wall ramp was strongly back-rotated as it was inverted up the upper 60° listric sector of the main detachment. This deformation produced significant thickness changes in the polymer above this back-rotated panel such that, together with the uplift of the ramp section, only a very gently tilted broad uplift formed in the syn-rift strata together with unfolding of the original syn-extension ramp syncline (Fig. 8b).

In a manner similar to that observed in the inverted 45° simple listric fault in Figure 8a, inversion deformation in the 60° ramp-flat fault system was significantly displaced or offset into the footwall by detachment in the polymer layer, and the development of inverted graben and thrusting at the footwall extremity (Fig. 8b).

The inversion of the listric fault systems with pre-extension polymer layers produced very different structures (Fig. 8a, b) to those formed by inversion of listric fault systems with no polymer layers (e.g. Fig. 7a, b). In particular, models with polymer layers were decoupled with inverted faults and new faults formed in the sub-polymer units, decoupling and thickness changes of the polymer layer, and folding of the supra-polymer stratigraphy. These models do not develop shortcut faults in the immediate footwall of the main detachment but, rather, part of the inversion deformation is translated/offset to the extremities of the footwall particularly where the polymer layer ends (Fig. 8a, b). Models with a polymer layer also show that the formation of primary polymer welds control the fold geometry of the inverted hanging-wall units (Fig. 8b).

Inversion of planar faults

Inversion of planar faults without a pre-extension polymer layer. The inversion geometries of planar fault models without a polymer layer in the pre-extension sand pack (Fig. 7c–e) are similar to those described by Buchanan & McClay (1991, 1992). Inversion of the 20° planar fault reactivated the main detachment, gently uplifting the hanging wall and producing a small frontal inversion anticline with a frontal-limb dip of approximately 15°, together with a broad zone of uplift of the syn-extensional strata above their regional and a very gentle back-limb dip of 5° (Fig. 7c). A shortcut thrust formed in the footwall of the main detachment and locally overturned the hanging-wall strata.

In contrast to the inversion of the 20° low-angle planar fault, inversion of the 60° planar and 60°–20° kinked planar faults produced well-developed asymmetric hanging-wall inversion anticlines with moderately dipping frontal limbs (38° and 35°, respectively) and gently dipping back limbs (20° and 18°, respectively) (Fig. 7d, e). Footwall shortcut faults developed within the sand pack in front of the inversion anticline. In both models, buttressing against the 60° dipping footwall produced new hanging-wall back-thrusts as inversion progresses. The syn-extension hanging-wall basin was progressively uplifted and small crestal-collapse graben developed on the outer arc of the asymmetrical inversion anticlines (Fig. 7d, e). The 60° ramp-flat kinked planar fault system has a shorter 60° dipping panel on the detachment surface (Fig. 7e), and this produced less hanging-wall uplift and a slightly smaller inversion anticline than the longer 60° panel in the simple 60° planar fault (Fig. 7d).

Inversion on planar faults with a pre-extension polymer layer. As for the listric faults, the inversion models of planar fault systems that had a pre-extension ductile polymer layer are characterized by decoupling of the sub-polymer and supra-polymer structures (Fig. 8c–e). In all of these Series 2 inverted planar fault models, the main detachment was reactivated and produced broad hanging-wall uplifts, together with changes in the polymer thickness, but the fault itself did not propagate though the polymer into the supra-polymer layers (Fig. 8c–e).

Inversion of the low-angle 20° planar fault model produced a very wide zone of hanging-wall uplift with the syn-extension strata uplifted above their regional. A low-relief asymmetrical frontal inversion anticline was only developed in the sub-polymer strata (Fig. 8c). In the very flat hanging wall of the inversion uplift, slight polymer thinning occurred together with polymer thickening into the distal hanging wall and into the footwall. The extensional graben structure near the end of the polymer layer in the footwall and the nearby strata are strongly deformed by thrusts detaching into the top of the polymer layer above the rigid footwall block (Fig. 8c). These thrusts, together with the thickened polymer section, indicate significant transfer of shortening from the reactivated 20° dipping planar fault into the footwall polymer layer and out to the left-hand edge of the model.

Inversion of the simple 60° planar fault model produced a broad zone of uplift above the main basin-bounding fault system under the polymer layer, with syn-extensional strata strongly uplifted and folded into a broad anticline tilted towards the footwall (Fig. 8d). Significant thickness changes occurred in the salt layer, with a well-developed primary weld in the hanging wall of the inverted sub-polymer graben next to the 60° fault. In the inverted hanging wall, a back-thrust developed above the polymer layer and carried the supra-polymer layers (including the syn-extensional strata) out of the original hanging-wall half-graben and over the footwall the main antithetic fault of the syn-extensional crestal-collapse graben (Fig. 8d). New hanging-wall-vergent back-thrusts formed as the result of buttressing against the steep footwall of the 60° planar fault. As in the inversion of the 20° planar fault described earlier, significant thickness changes occurred in the polymer layer with the weld where the polymer was totally thinned with polymer migration into the half-graben axis and distal hanging wall, as well as into the footwall (Fig. 8d). Here, above the rigid footwall, silicone inflation occurred in addition to contraction of the graben near the end of the footwall polymer layer (Fig. 8d). These features indicate significant displacement and strain transfer from the hanging-wall inversion into the footwall units. As in all of the Series 2 inversion models with a pre-extension ductile layer, the main inverted basin-bounding fault did not penetrate upwards into the supra-polymer section (Fig. 8).

Inversion of the 60°–20° kinked planar fault system produced a broad, more symmetrical anticline above the inverted sub-polymer half-graben (Fig. 8e). A crestal-collapse graben formed on the apex of the broad inversion uplift. Several small, back-thrusts formed as a result of buttressing against the steep 60°-dipping part of the main detachment surface (Fig. 8e). As for all of the other models described above, transfer of displacement and strain from the hanging wall into the distal footwall resulted in thickening of the polymer layer in the hanging wall and also in the footwall. The small half-graben that formed near the end of the polymer detachment during extension was strongly shortened by the inversion (Fig. 8e).

Figure 9 shows the progressive evolution of the 60° planar fault model with a pre-extension polymer layer. At the end of extension, the structure was a broad hanging-wall syncline of syn-extension strata decoupled from the faulted half-graben below the salt layer (Fig. 9a). The progressive inversion is tracked in Figure 9 from the uplift and partial unfolding of the syn-extensional strata (Fig. 9b), and the development of the back-thrust overlying the polymer layer (Fig. 9c), to the eventual formation of the polymer primary weld (Fig. 9d). Concordant with the structural decoupling–folding and detachment thrusting above the polymer layer, and the reactivation of the extensional faults and new back-thrusts beneath the polymer layer, the polymer shows migration from the corner regions of the main sub-polymer faults into both the footwall in front of the inverted half-graben and the hanging wall (Fig. 9c, d).

Discussion

In this section, the results of the analogue models are analysed and compared to natural examples of inverted extensional basin that contain salt or evaporite layers. The structural styles of the Series 1 sandbox models that did not contain viscous layers in the hanging-wall stratigraphy are compared to Series 2 models that had viscous layers (Table 1).

Role of a viscous layer during model extension

The kinematic evolution and fault/fold styles of the analogue models during the extension were mainly controlled by the geometry of the main basin-bounding fault geometry, as well as by the presence or absence of a weak, ductile viscous layer within in the pre-kinematic sequence (Figs 4–9).

Series 1 models without a viscous layer

The results of the Series 1 extension baseline models with a rigid footwall block and an isotropic sand pack (Fig. 4) are comparable to sandbox models described in the literature (e.g. McClay & Ellis 1987*a*, *b*; Ellis & McClay 1988; McClay 1990; McClay *et al.* 1991) (Fig. 1). As in previous experiments, the hanging-wall geometries above the main basin-bounding fault are controlled by the dip and shape of the fault surface (Fig. 4), as well as by the amount of extension. Models where the fault surface was kinked or had a ramp-flat geometry produced both hanging-wall rollover anticlines and synclinal geometries (e.g. Fig. 4b, e). In the Series 1 models presented in this paper, planar antithetic faults were mainly developed where the main basin-bounding fault dipped by more than 45° at the break-away (Fig. 4b, d, e) (cf. McClay 1990). The Series 1 isotropic models are coupled in the sense that the extensional faults affect both the pre-kinematic and syn-kinematic units.

Series 2 models with a viscous layer

The deformation of Series 2 models typically formed decoupled architectures, with the supra-polymer strata folded into hanging-wall growth synclines above the basin-bounding faults (Figs 5 & 6). The units below the polymer layer formed half-graben. Where the initial breakaway dip of the principal fault was greater than 45°, strains in the half-graben were accommodated by steep antithetic faults (Figs 5b, d, e & 6). Similar decoupled hanging-wall deformation in analogue models with polymer layers was described by Soto *et al.* (2007) and Ferrer *et al.* (2008*b*, 2014).

Extension was accommodated by differential viscous flow of the polymer across the footwall of the basin-bounding fault, thickening into the hanging wall and thinning across the edge of the footwall. In most of the models, the polymer layer remained continuous (Fig. 5a–c, e), whereas, in the 60° planar fault model, polymer flow into the half-graben across the footwall of the antithetic fault at the rollover hinge produced a primary polymer weld (Figs 5d & 6d). At this stage, this section of the model became coupled and a small extensional fault formed in the supra-polymer strata just to the right of the weld (Fig. 6d).

In these models, the hanging-wall basins above the polymer were all synclinal in form, with the width and depth reflecting the changes in thickness of the polymer layer (Fig. 5). The simple 45° listric fault model (Fig. 5a) and the gently-dipping 20° planar fault model (Fig. 5c) formed wide, gentle supra-polymer basins with only subtle changes in the thickness of the polymer, whereas models with steeper fault dips on the basin-bounding faults (Fig. 5b, d, e) developed deeper synclinal basins underlain by significant changes in the thickness of the polymer. In these models, there was significant polymer flow into the hanging-wall graben particularly for the 60° planar fault model (Figs 5d & 6).

In the Series 1 models, deformation above the footwall block produced narrow extensional graben towards the end of the polymer layer (Fig. 5). Footwall extensional strains were transmitted along the polymer detachment, localizing faulting near the end of the polymer unit (cf. also Vendeville & Jackson 1992; Jackson & Vendeville 1994). Complex narrow graben developed as extension progressed (Fig. 6). The addition of syn-kinematic sand layers during continued extension inhibited the formation of reactive polymer diapirs within these graben.

Role of a viscous layer during inversion of the models

Inversion of analogue models with rigid footwall blocks was investigated by McClay (1989, 1995), Buchanan & McClay (1991, 1992), Keller & McClay (1995), and Yamada & McClay (2003*a*, *b*) (Fig. 1b, d). These experiments did not have any very weak layers in the hanging-wall strata. These models formed classic harpoon structures with reactivation and upwards propagation of the basin-bounding fault, and uplift and back-rotation of the syn-extension strata with part remaining in net extension (Fig. 1b, d). In the Series 1 models discussed in this paper, contraction (5 cm) exceeded extension (3 cm) such that most of the syn-extension strata were uplifted above regional during the inversion (Fig. 7). The depth slices and sections of Figure 10 show that there were only a few footwall shortcut thrusts formed in the lower part of the tilted front limb of the inversion anticline. The inverted faults were approximately linear, as were the back-thrusts, and there was no deformation in the main part of the footwall strata (Fig. 10b, d).

The models of the Series 2 experiments with a polymer layer show strong decoupling between the sub- and supra polymer layers (Figs 8 & 11). Broad gentle folding developed above the polymer layer, with the polymer thickened beneath the anticlines and depleted under the synclines (Figs 8, 9 & 11a, c). The depth slices clearly show the folded hanging-wall strata (Fig. 11b, d), in strong contrast to the dominance of linear hanging-wall fault arrays and the absence of footwall deformation in the Series 1 baseline models (Fig. 10b, d).

The inherited polymer configuration at the end of extension and, particularly, the positions of primary welds was critical during inversion because these disrupted the polymer within the model. Similarly, where welds formed during inversion (e.g. Figs 8a, b, d, e & 9d) strongly controlled the inversion architectures in the last stage of net contraction. In the region of the welds, shortening in the sub-polymer strata was transferred into the supra-polymer strata enhancing uplift, forward tilting and folding of the syn-extensional stratigraphy (e.g. Figs 8d, e & 9). The resultant outer-arc stretching in these uplifted zones produced inversion-related crestal-collapse graben within the syn-extensional units (Figs 8e & 11a).

Natural examples of extension and inverted basins with salt layers

The results of the analogue models of inverted extensional basins with an internal ductile detachment layer are compared with natural examples of inverted basins from the Parentis Basin in the Bay of Biscay, from the Central and Southern North Sea basins, and from the Cameros Basin in the Iberian Range, central Spain.

Parentis Basin, Bay of Biscay

The Parentis Basin in the eastern Bay of Biscay is a partly inverted extensional basin with salt units in the pre-rift section (Roca *et al.* 2011; Ferrer

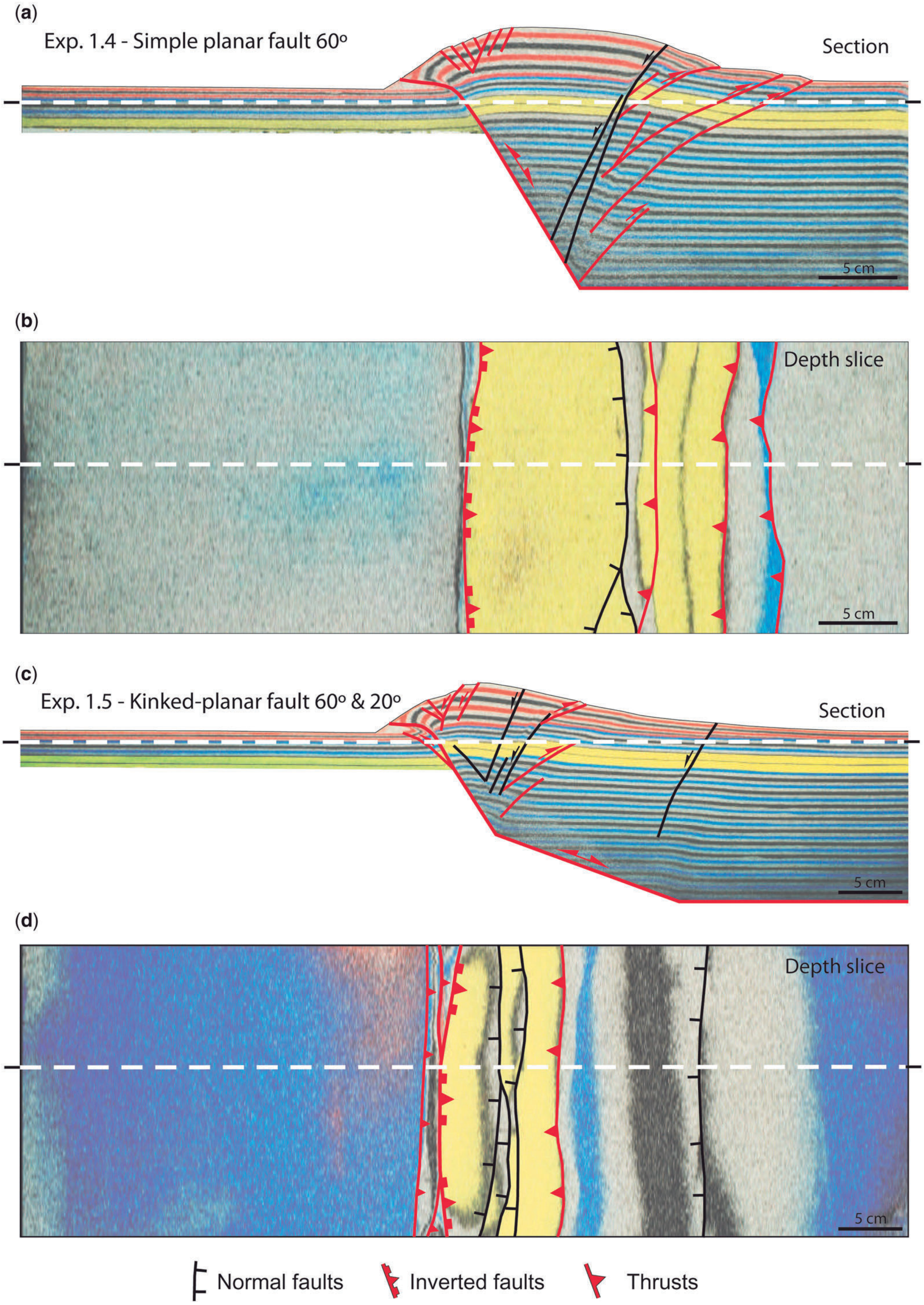

Colour online/ colour hardcopy

Fig. 10. Interpreted section and depth slices through reconstructed volumes of baseline isotropic experiments: (**a**) & (**b**) with a simple planar fault dipping 60°; and (**c**) & (**d**) with a 60°–20° kinked-planar fault. White dashed lines indicate the location of each depth slice on the cross-sections and vice versa.

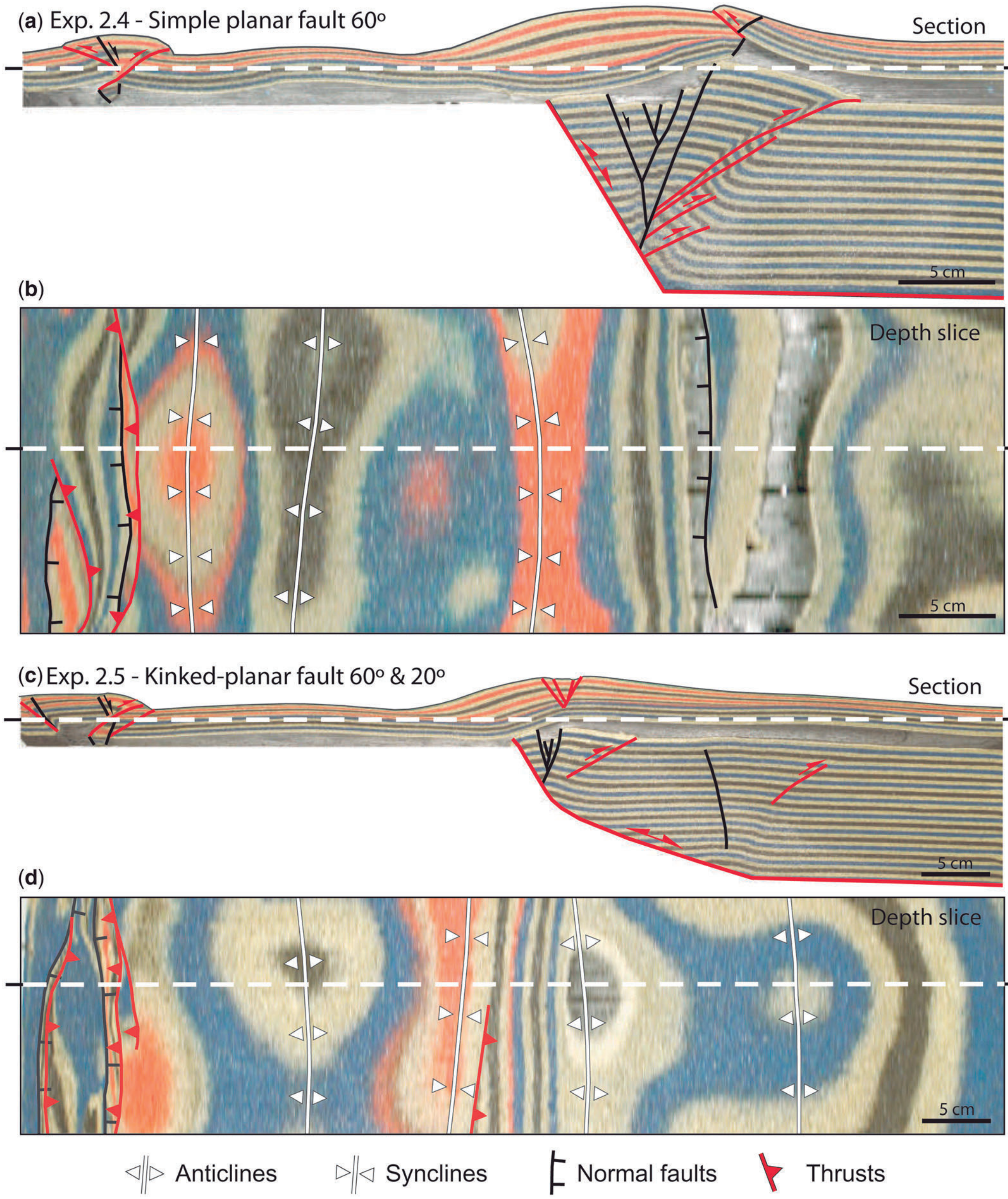

Colour online/colour hardcopy

Fig. 11. Interpreted section and depth slices through reconstructed volumes of anisotropic experiments: (**a**) & (**b**) with a simple planar fault dipping 60°; and (**c**) & (**d**) with a 60°–20° kinked-planar fault. White dashed lines indicate the location of each depth slice on the cross-sections and vice versa.

et al. 2012; Rowan 2014). This Late Jurassic–Lower Cretaceous basin is part of a series of east–west-trending rift basins developed between Iberia and Europe during the opening of the Bay of Biscay and the North Atlantic (Srivastava *et al.* 1990). Whereas most of the Pyrenean basins were subsequently strongly inverted during the Late Cretaceous–Cenozoic Pyrenean Orogeny (e.g. Berástegui *et al.* 1990; Muñoz 1992; Bond & McClay 1995; García-Senz 2002; Mencos 2011; Roca *et al.* 2011), the Parentis Basin was only slightly inverted because of buttressing produced by a major basement high located to the south (Ferrer *et al.* 2008*a*). The present-day structure of the

Parentis Basin was controlled by two east–west-trending, north-dipping low-angle crustal extensional faults and by the presence of Upper Triassic evaporites. This Triassic salt unit is considered pre-rift in relation to the main Late Jurassic–Lower Cretaceous rifting and the opening of the Bay of Biscay (Rowan 2014).

The structure of the Parentis Basin is characterized by a growth syncline controlled by thick-skinned extension that triggered salt migration (Ferrer *et al.* 2012) (Fig. 12a). During the extension, the salt partially decoupled the major sub-salt fault from the supra-salt cover units (Ferrer *et al.* 2012). The experimental model in Figure 5e has a basement structure of a kinked planar detachment fault that is inferred to represent the extensional architecture of the Parentis Basin, which has been derived from seismic sections and cross-section restorations. In the Parentis Basin, the Barremian–Lower Aptian syn-rift strata in the hanging-wall

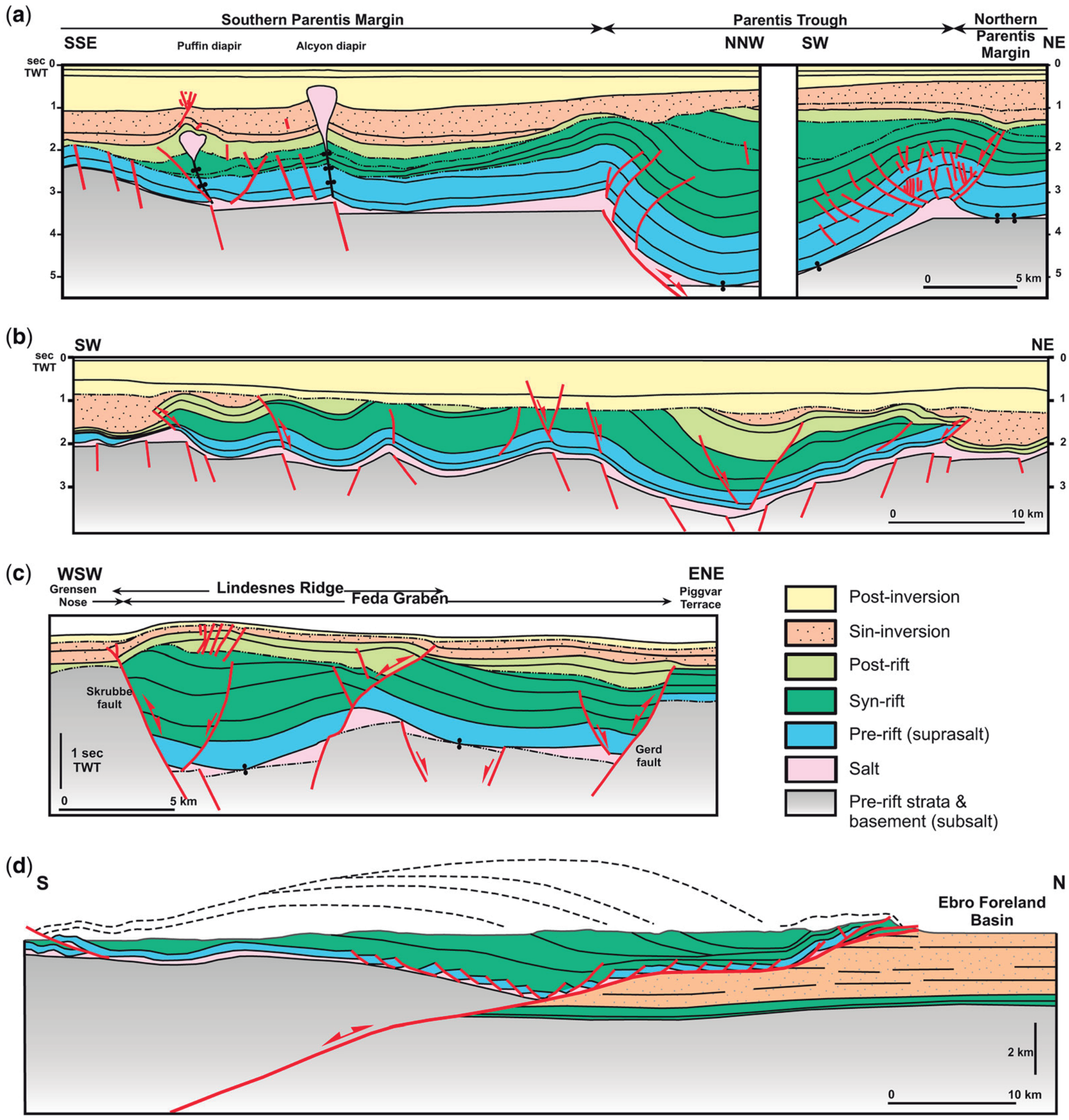

Colour online/ mono hardcopy

Fig. 12. Natural examples of inverted basins containing pre-kinematic salt units and with different degrees of shortening–inversion. (**a**) Geoseismic section of part of the Parentis Basin (eastern Bay of Biscay) (modified from Ferrer *et al.* 2012). (**b**) Line drawing of a seismic section of the central Broad Fourteens Basin (southern North Sea) (modified from Nalpas *et al.* 1995). (**c**) Simplified geoseismic section from the southern Feda Graben (North Sea) (modified from Gowers *et al.* 1993). (**d**) Cross-section of the Cameros Basin, Iberian chain, Spain (modified from Soto *et al.* 2007). TWT, two-way time.

syncline onlap towards the south (Fig. 12a) in a fashion similar to that displayed in the analogue model (Fig. 5e). The Pyrenean Late Cretaceous–Cenozoic inversion of the basin-bounding fault produced uplift of the depocentre, as shown by the different regional levels for the lower syn-inversion top Paleocene and Eocene strata both in the hanging wall and in the footwall. A similar feature is seen in the experimental models (Fig. 8e). The Parentis Basin also shows diapirs and salt walls developed above the footwall of the major fault (Fig. 12a). However, similar structures were not developed in the sandbox models presented in this paper, most probably related to the lesser extension in the models and, perhaps, to greater initial salt thicknesses in the Parentis Basin. In the Parentis Basin section (Fig. 12a), the presence of basement faults below the salt walls could also be an important factor, with salt preferentially absorbing the contractional deformation, squeezing the salt diapirs and forming secondary welds (Ferrer *et al.* 2012). In contrast, in the analogue models, the contractional deformation resulted in graben inversion or the development of new thrusts verging in the same direction as the major graben-bounding fault (Fig. 8).

Broad Fourteen Basin, Dutch sector, Southern North Sea Basin

The Broad Fourteens Basin in the Dutch sector of Southern North Sea shows very spectacular examples of positive inversion, with thrusts faults at the basin margins related to the Zechstein (Upper Permian) salt that acted as a major detachment during inversion (e.g. Nalpas *et al.* 1995) (Fig. 12b). The geological history of this basin was controlled by halokinesis and minor extension until the Mid-Jurassic followed by Mid to Late Jurassic NE–SW extension and Cretaceous post-rift subsidence (Van Wijhe 1987). In the Late Cretaceous (Senonian), the collision between the African Plate and the European Plate (Alpine Orogeny) produced far-field hinterland contraction to the north and inversion of the Broad Fourteens Basin (Ziegler 1975, 1982; Van Wijhe 1987). This resulted in folding, uplift and erosion (Nalpas *et al.* 1995). The southern sector of the basin contains no salt, no decoupling and the inverted basement faults have propagated through the overlying sedimentary section (Nalpas *et al.* 1995). In contrast, the northern sector of the basin contains Zechstein salt with the inversion structures controlled by the salt thickness (Fig. 12b). On the SW margin of the basin, broad detachment folds formed above the Zechstein salt: on the NE margin, however, a low-angle thrust fault detached on top of the salt has carried the supra-salt section onto the footwall of the extensional basin (Fig. 12b). The experiments of Ferrer *et al.* (2014) indicate that at the end of the extension these structures may have initiated on salt inflations or salt-ridges with the basinward-dipping inversion faults detached on top of the salt. The sandbox models presented in this paper have less inversion compared to that in the Broad Fourteens Basin: however, it is possible to envisage how the hanging wall of the basin-margin fault above the salt was transported over the footwall during inversion (e.g. Fig. 11).

Feda Graben, Danish North Sea

The inverted Feda Graben (Fig. 12c) at the Norwegian–Danish boundary of the North Sea Central Graben Basin exhibits similar inversion structures to those formed above an inverted planar fault system with salt layers (Figs 8d & 9). The geo-history of this part of the North Sea includes pre-rift Late Permian Zechstein salt, Mid–Late Jurassic rifting and a later Cretaceous–Early Tertiary inversion (Gowers & Sæbøe 1985; Gowers *et al.* 1993; Taylor 1998; Tanveer & Korstgård 2009). The Feda Graben is bounded by two NNW-trending basement faults (Gowers & Sæbøe 1985) – the Skrubbe Fault that separates the basin from the Grensen Nöse in the SW and the Gert Fault that separates the basin from the Piggvar Terrace in the NE (Fig. 12c). This simplified sketch section can be compared to Figure 8d, where the axial syncline of the pre-extensional strata was controlled by polymer migration during extension, and the antiformal shape (Lindesnes Ridge: Skjerven *et al.* 1983) of the Cretaceous–Cenozoic units in the central part of the Feda Graben is clearly related to the inversion of the main Skrubbe Fault (Fig. 12c). Figures 8d and 9 show similar features with buttressing against the main bounding fault transferring deformation into the centre of the graben system, as seen in the Feda Graben in Figure 12c. During extension in the sandbox model, a normal fault detached on the polymer developed above the rollover hinge (Fig. 6). Inversion produced asymmetric uplift of the synclinal basin as a result of buttressing against the basin-bounding fault. Part of the contractional deformation was transmitted by the weak polymer to the distal edge of the basin where the small graben system was inverted with a new intra-graben reverse fault (Fig. 9).

Cameros Basin, Iberian Range, Spain

The Cameros Basin in the NW Iberian range in Spain (Guimerà & Álvaro 1990; Casas & Salas 1992; Salas & Casas 1993; Guimerà *et al.* 1995; Casas *et al.* 2009; Mas *et al.* 2011; Omodeo Salé *et al.* 2014) is one of the NW–SE-striking intraplate

Mesozoic rift basins related to the opening of Western Tethys and the North Atlantic Ocean (Álvaro *et al.* 1979). From the Late Jurassic to the Early Albian, the Cameros Basin underwent major subsidence, with the deposition of more than 6 km of syn-rift strata overlying the pre-rift section of Upper Triassic evaporites and Jurassic limestones (Mas *et al.* 2011). Various models have been proposed to explain the geometry of this basin (e.g. the review by Omodeo Salé *et al.* 2014). The analogue model results presented in this paper (Figs 5a & 8a) support a hanging-wall synclinal model, as proposed by Casas & Salas (1992), Casas *et al.* (2000~~, 2009~~) and Soto *et al.* (2007). This suggests that the hanging-wall synclinal basin with syn-kinematic extensional growth strata resulted from extension of a major south-dipping listric fault with an Upper Triassic evaporite detachment (Fig. 12d) in a manner similar to that shown in the sandbox model (Fig. 5a). In the Eocene–Early Miocene, the Cameros Basin was totally inverted as a result of the Alpine Orogeny (Guimerà & Álvaro 1990; Salas & Casas 1993; Guimerà *et al.* 1995). During the inversion, the Upper Triassic evaporites acted as a detachment (Guimerà & Álvaro 1990), thrusting the extensional hanging-wall synclinal basin over the Cenozoic Ebro foreland basin with a maximum displacement of around 30 km (Casas-Sainz & Simón-Gómez 1992) (Fig. 12d). The resulting inverted basin is very analogous to the inverted listric fault model shown in Figure 8a.

Conclusions

The results of the analogue modelling programme presented in this paper provide both geometrical and kinematic templates that may be applied to the analysis of the structural evolution of normal faults involving pre-extensional evaporites (particularly salt layers) and then subsequently inverted. The shapes of the basement-bounding faults controlled the geometries of the supra-'salt' synclinal basins formed during the extensional deformation, and the location of fault-propagation folds and supra-'salt' decoupling during inversion. Wide, gentle and shallow synclinal supra-'salt' basins developed in the models during extension in the hanging wall of a simple listric or gently dipping simple planar fault (Fig. 5a, c). In contrast, narrow and deep synclinal extensional basins developed above steeply dipping planar faults (Figs 5d & 6) or the ramps of a ramp-flat listric faults (Fig. 5b) in the models. The development of the hanging-wall synclinal basins was also controlled by polymer migration towards the edges of the basin below where salt-inflated areas developed at the end of the extension (Fig. 5b, d, e).

The inherited extensional architectures both in the analogue models and in the natural examples exert a fundamental role during later inversion. In the models, shortening preferentially inverted the major basement basin-bounding faults and the polymer layer acted as a contractional detachment transferring the deformation above the footwall. Independently of the basement fault geometry, the hanging-wall synclinal basins were arched and uplifted during the inversion, and partially translated over the rigid footwall. The uplift of the synclinal basins was accelerated when primary welds developed under the main synclinal basins depocentres during the late stages of inversion.

The experimental results also show the development of extensional graben at the extremities of the footwall strata and these were later inverted.

The presence of pre-rift evaporites controls the structural style of the supra- and sub-salt units. Whereas strata below the polymer can be strongly faulted, continuous deformation characterized by folded synclinal basins formed above the polymer or salt layer. In this sense, the presence of a polymer layer (or salt in nature) acts as an effective decoupling unit inhibiting the upwards propagation of the faults from the sub-salt to the supra-salt layers during both extension and inversion.

The main limitation of analogue models that used a rigid block to control the geometry of the basin-bounding fault systems is that it limited the footwall deformation to the ductile layer and the overlying footwall strata. Despite this, the sandbox models produce many strikingly similar deformation features to those found in natural examples of inverted basins with salt strata, as described in this paper.

This research was funded by the STAR Research Consortium, sponsored by BG Group, BHPBilliton, ConocoPhilips, Eni, MarathonOil, Nexen, Shell, Talisman Energy and YFP. The authors also received additional support from the Fault Dynamics Research Group, Royal Holloway University of London. We also thank Kevin D'Souza, Jerry Morris and Frank Lehane for the logistical support in the modelling laboratory. Research of OF was partially supported by the SALTECRES project (CGL2014-54118-C2-1-R), as well as the Grup de Recerca de Geodinàmica i Anàlisi de Conques (2014SGR467). Reviews and suggested improvements by S. Buiter, I.A. Alsop and C. Childs were greatly appreciated.

References

Álvaro, M., Capote, R. & Vegas, R. 1979. Un modelo de evolución geotectónica para la cadena Celtibérica. *Acta Geologica Hispana*, **14**, 172–181.

Bally, A.W. 1984. Tectonogénese et sismique de réflexion. *Bulletin Société Géologique de France*, **7**, 279–285.

Berástegui, X., García-Senz, J. & Losantos, M. 1990. Tecto-sedimentary evolution of the Organyà extensional basin (central south Pyrenean unit, Spain) during the Lower Cretaceous. *Bulletin Societé Géologique France*, **8**, 251–264.

Bond, R.M.G. & McClay, K.R. 1995. Inversion of a Lower Cretaceous extensional basin, south central Pyrenees, Spain. *In*: Buchanan, J.G. & Buchanan, P.G. (eds) *Basin Inversion*. Geological Society, London, Special Publications, **88**, 415–431, http://doi.org/10.1144/GSL.SP.1995.088.01.22

Bonini, M., Sani, F. & Antonielli, B. 2012. Basin inversion and contractional reactivation of inherited normal faults: a review based on previous and new experimental models. *Tectonophysics*, **522–523**, 55–88.

Brun, J.-P. & Nalpas, T. 1996. Graben inversion in nature and experiments. *Tectonics*, **15**, 677–687.

Buchanan, P.G. & McClay, K.R. 1991. Sandbox experiments of inverted listric and planar fault systems. *Tectonophysics*, **188**, 97–115.

Buchanan, P.G. & McClay, K.R. 1992. Experiments on basin inversion above reactivated domino faults. *Marine and Petroleum Geology*, **9**, 486–500.

Buiter, S.H.J., Pfiffner, O.A. & Beaumont, C. 2009. Inversion of extensional sedimentary basins: a numerical evaluation of the localization of shortening. *Earth and Planetary Sciences Letters*, **288**, 492–504.

Burliga, S., Koyi, H.A. & Krzywiec, P. 2012. Modelling cover deformation and decoupling during inversion, using the Mid-Polish Trough as a case study. *Journal of Structural Geology*, **42**, 62–73.

Butler, R.W.H., Maniscalco, R., Sturiale, G. & Grasso, M. 2014. Stratigraphic variations control deformation patterns in evaporite basins: Messinian examples, onshore & offshore Sicily (Italy). *Journal of the Geological Society, London*, **172**, 113–124, http://doi.org/10.1144/jgs2014-024

Casas, A. & Salas, R. 1992. Historia de la subsidencia, anomalías gravimétricas y evolución mesozoica de las Cuencas del margen oriental de Iberia. *In*: *Actas de las sesiones científicas: III Congreso Geológico de España*. Facultad de Ciencias, Universidad de Salamanca, Salamanca, 112–116.

Casas, A.M., Villalaín, J.J., Soto, R., Gil-Imaz, A., Del Río, P. & Fernández, G. 2009. Multidisciplinary approach to an extensional syncline models for the Mesozoic Cameros Basin (N Spain). *Tectonophysics*, **470**, 3–20.

Casas-Sainz, A.M. & Simón-Gómez, J.L. 1992. Stress field and thrust kinematics: a model for the tectonic inversión of the Cameros massif (Spain). *Journal of Structural Geology*, **14**, 521–530.

~~EDQ1~~ Casas-Sainz, A.M., Cortés-Gracia, A.L. & Maestro-González, A. 2000. Intra-plate deformation and basin formation during Tertiary at the Northern Iberian Plate: origin and evolution of the Almazán Basin. *Tectonics*, **19**, 762–786.

Corti, G. 2012. Evolution and characteristics of continental rifting: analog modeling-inspired view and comparison with examples from the East African Rift System. *Tectonophysics*, **522–523**, 1–33.

Coward, M. & Stewart, S. 1995. Salt-influenced structures in the Mesozoic-Tertiary cover of the Southern North Sea, U.K. *In*: Jackson, M.P.A., Roberts, D.G. & Snelson, S. (eds) *Salt Tectonics: A Global Perspective*. American Association of Petroleum Geologists, Memoirs, **65**, 229–250.

Dell'Ertole, D. & Schellart, W.P. 2013. The development of sheath folds in viscously stratified materials in simple shear conditions: an analogue approach. *Journal of Structural Geology*, **56**, 129–141.

Del Ventisette, C., Montanari, D., Sani, F. & Bonini, M. 2006. Basin inversion and fault reactivation in laboratory experiments. *Journal of Structural Geology*, **28**, 2067–2083.

Dooley, T., McClay, K.R., Hempton, M. & Smit, D. 2005. Salt tectonics above complex basement extensional fault systems: results from analogue modelling. *In*: Doré, E.G. & Vining, B.A. (eds) *Petroleum Geology: North-West Europe and Global Perspectives – Proceedings of the 6th Petroleum Geology Conference*. Geological Society, London, 1631–1648, http://doi.org/10.1144/0061631

Dooley, T., Jackson, M.P.A., Jackson, C.A.L., Hudec, M.R. & Rodriguez, C.R. 2015. Enigmatic structures within salt walls of the Santos Basin – Part 2: mechanical explanation from physical modeling. *Journal of Structural Geology*, **75**, 163–187.

Dubois, A., Odonne, F., Massonnat, G., Lebourg, T. & Fabre, R. 2002. Analogue modelling of fault reactivation: tectonic inversion and oblique remobilization of grabens. *Journal of Structural Geology*, **24**, 1741–1752.

Ellis, P.G. & McClay, K.R. 1988. Listric extensional fault systems-results of analogue model experiments. *Basin Research*, **1**, 55–70.

Ferrer, O., Roca, E., Benjumea, B., Muñoz, J.A., Ellouz, N. & Marconi Team 2008*a*. The deep seismic reflection MARCONI-3 profile: role of extensional Mesozoic structure during Pyrenean contractional deformantion at the Eastern part of the Bay of Biscay. *Marine and Petroleum Geology*, **25**, 714–730.

Ferrer, O., Roca, E. & Vendeville, B.C. 2008*b*. Influence of a syntectonic viscous salt layer on the structural evolution of extensional kinked-fault systems. *Bollettino di Geofisica Teorica ed Applicata*, **49**, 371–375.

Ferrer, O., Jackson, M.P.A., Roca, E. & Rubinat, M. 2012. Evolution of salt structures during extension and inversion of the offshore Parentis Basin (eastern Bay of Biscay). *In*: Alsop, G.I., Archer, S.G., Hartley, A.J., Grant, N.T. & Hodgkinson, R. (eds) *Salt Tectonics, Sediments and Prospectivity*. Geological Society, London, Special Publications, **363**, 361–379, http://doi.org/10.1144/SP363.16

Ferrer, O., Roca, E. & Vendeville, B.C. 2014. The role of salt layers in the hangingwall deformation of kinked-planar extensional faults: insights from 3D analogue models and comparison with the Parentis Basin. *Tectonophysics*, **636**, 338–350.

Fiduk, J.C. & Rowan, M.G. 2012. Analysis of folding and deformation within layered evaporites in Blocks BM-S-8 and -9, Santos Basin, Brazil. *In*: Alsop, G.I., Archer, S.G., Hartley, A.J., Grant, N.T. & Hodgkinson, R. (eds) *Salt Tectonics, Sediments and Prospectivity*. Geological Society, London, Special Publications, **363**, 471–487, http://doi.org/10.1144/SP363.22

García-Senz, J. 2002. *Cuencas extensivas del Cretácico Inferior en los Pirineos Centrales, formación, y subsecuente inversión*. PhD thesis, Universitat de Barcelona.

Gowers, M.B. & Sæbøe, A. 1985. On the structural evolution of the central trough in the Norwegian and Danish sectors of the North Sea. *Marine and Petroleum Geology*, **2**, 298–318.

Gowers, M.B., Holtar, E. & Swensson, E. 1993. The structure of the Norwegian Central Trough (Central Graben area). *In*: Parker, J.R. (ed.) *Petroleum Geology of Northwest Europe: Proceedings of the 4th Conference*. Geological Society, London, 1245–1254, http://doi.org/10.1144/0041245

Guimerà, J. & Álvaro, M. 1990. Structure et évolution de la compression alpine dans la Chaîne Ibérique et la Chaîne côtière catalane (Espagne). *Bulletin de la Société Géologique France*, **VI**, 339–348.

Guimerà, J., Alonso, A. & Mas, J.R. 1995. Inversion of an extensional-ramp basin by a newly formed thrust: the Cameros basin (N Spain). *In*: Buchanan, J.G. & Buchanan, P.G. (eds) *Basin Inversion*. Geological Society, London, Special Publications, **88**, 433–453, http://doi.org/10.1144/GSL.SP.1995.088.01.23

Horsfield, W.T. 1977. An experimental approach to basement controlled faulting. *Geologie en Mijnbouw*, **56**, 363–370.

Huiqi, L., McClay, K.R. & Powell, D. 1992. Physical models of thrusts wedges. *In*: McClay, K.R. (ed.) *Thrust Tectonics*. Chapman and Hall, London, 71–81.

Jackson, M.P.A. & Vendeville, B.C. 1994. Regional extension as a geological trigger for diapirism. *Geological Society of America Bulletin*, **106**, 57–73.

Jackson, M.P.A., Cornelius, R.R., Craig, C.R., Gansser, A., Stöcklin, J. & Talbot, C.J. 1990. *Salt Diapirs of the Great Kavir, Central Iran*. Geological Society of America, Memoirs, **177**.

Keller, J.V.A. & McClay, K.R. 1995. 3D sandbox models of positive inversion. *In*: Buchanan, J.G. & Buchanan, P.G. (eds) *Basin Inversion*. Geological Society, London, Special Publications, **88**, 137–146, http://doi.org/10.1144/GSL.SP.1995.088.01.09

Koyi, H., Jenyon, M.K. & Petersen, K. 1993. The effect of basement faulting on diapirism. *Journal of Petroleum Geology*, **163**, 285–312.

Krantz, R.W. 1991. Measurements of friction coefficients and cohesion for faulting and fault reactivation in laboratory models using sand and sand mixtures. *Tectonophysics*, **188**, 203–207.

Krzywiec, P. 2006. Structural inversion of the Pomeranian and Kuiavian segments of the Mid-Polish Trough – lateral variations in timing and structural style. *Geological Quarterly*, **50**, 151–168.

Letouzey, J., Colleta, B., Vially, R. & Chermette, J.C. 1995. Evolution of salt-related structures in compressional settings. *In*: Jackson, M.P.A., Roberts, D.G. & Snelson, S. (eds) *Salt Tectonics: A Global Perspective*. American Association of Petroleum Geologists, Memoirs, **65**, 41–60.

Lohrmann, J., Kukowski, N., Adam, J. & Oncken, O. 2003. The impact of analogue material properties on the geometry, kinematics, and dynamics of convergent sand wedges. *Journal of Structural Geology*, **25**, 1691–1711.

Mas, R., Benito, M.I. *et al.* 2011. Evolution of an intraplate rift basin: the Latest Jurassic-Early Cretaceous Cameros Basin (Northwest Iberian Ranges, North Spain). *In*: Arenas, C., Pomar, L. & Colombo, F. (eds) *Post-Meeting Field Trips 28th IAS Meeting*. *Geo-Guías*, **8**, 117–154.

McClay, K.R. 1989. Analogue models of inversion tectonics. *In*: Cooper, M.A. & Williams, G.D. (eds) *Inversion Tectonics*. Geological Society, London, Special Publications, **44**, 41–59, http://doi.org/10.1144/GSL.SP.1989.044.01.04

McClay, K.R. 1990. Deformation mechanics in analogue models of extensional fault systems. *In*: Rutter, E.H. & Knipe, R.J. (eds) *Deformation Mechanisms, Rheology and Tectonics*. Geological Society, London, Special Publications, **54**, 445–454, http://doi.org/10.1144/GSL.SP.1990.054.01.40

McClay, K.R. 1995. The geometries and kinematics of inverted fault systems: a review of analogue models studies. *In*: Buchanan, J.G. & Buchanan, P.G. (eds) *Basin Inversion*. Geological Society, London, Special Publications, **88**, 97–118, http://doi.org/10.1144/GSL.SP.1995.088.01.07

McClay, K.R. & Buchanan, P.G. 1992. Thrust faults in inverted extensional basins. *In*: McClay, K.R. (ed.) *Thrust Tectonics*. Chapman & Hall, London, 419–434.

McClay, K.R. & Ellis, P.G. 1987*a*. Analogue models of extensional fault geometries. *In*: Coward, M.P., Dewey, J.F. & Hancock, P.L. (eds) *Continental Extensional Tectonics*. Geological Society, London, Special Publications, **28**, 109–125, http://doi.org/10.1144/GSL.SP.1987.028.01.09

McClay, K.R. & Ellis, P.G. 1987*b*. Geometries of extensional fault systems developed in model experiments. *Geology*, **15**, 341–344.

McClay, K.R. & Scott, A.D. 1991. Experimental models of hangingwall deformation in ramp-flat listric extensional fault systems. *Tectonophysics*, **188**, 85–96.

McClay, K.R., Waltham, D.A., Scott, A.D. & Abousetta, A. 1991. Physical and seismic modelling of listric normal fault geometries. *In*: Roberts, A.M., Yielding, G. & Freeman, B. (eds) *The Geometry of Normal Faults*. Geological Society, London, Special Publications, **56**, 231–239, http://doi.org/10.1144/GSL.SP.1991.056.01.16

Mencos, J. 2011. *Metodologies de reconstrucció i modelització 3D d'estructures geològiques: anticlinal de Sant Corneli – Bóixols (Pirineus Centrals)*. PhD thesis. Universitat de Barcelona.

Muñoz, J.A. 1992. Evolution of a continental collision belt: ECORS-Pyrenean crustal balanced section. *In*: McClay, K.R. (ed.) *Thrust Tectonics*. Chapman & Hall, London, 235–246.

Nalpas, T. & Brun, J.P. 1993. Salt flow and diapirism related to extension at crustal scale. *Tectonophysics*, **28**, 349–362.

Nalpas, T., Le Douaran, S., Brun, J.-P., Unternehr, P. & Richert, J.-P. 1995. Inversion of the Broad Fourteens Basin (offshore Netherlands), a small-scale model investigation. *Sedimentary Geology*, **95**, 237–250.

Omodeo Salè, S., Gumerà, J., Mas, R. & Arribas, J. **EDQ2**
2014. Tectono-stratigraphic evolution of an inverted

extensional basin: the Cameros Basin (north of Spain). *International Journal Earth Science (Geologische Rundschau)*, **103**, 1597–1620.

Panien, M., Schreurs, G. & Pfiffner, A. 2005. Sandbox experiments on basin inversion: testing the influence of basin orientation and basin fill. *Journal of Structural Geology*, **27**, 433–445.

Panien, M., Buiter, S.J.H., Schreurs, G. & Pfiffner, O.A. 2006. Inversion of a symmetric basin: insights from a comparison between analogue and numerical experiments. *In*: Buiter, S.J.H. & Schreurs, G. (eds) *Analogue and Numerical Modelling of Crustal-Scale Processes*. Geological Society, London, Special Publications, **253**, 253–270, http://doi.org/10.1144/GSL.SP.2006.253.01.13

Roca, E., Muñoz, J.A., Ferrer, O. & Ellouz, N. 2011. The role of the Bay of Biscay Mesozoic extensional structure in the configuration of the Pyrenean orogeny: constraints from the MARCONI deep seismic reflection survey. *Tectonics*, **30**, TC2001.

Rowan, M.G. 2014. Passive-margin salt basins: hyper-extension, evaporite deposition, and salt tectonics. *Basin Research*, **26**, 154–182.

Rowan, M.G. & Krzywiec, P. 2014. The Szamotuly salt diapir and Mid-Polish Trough: decoupling during both Triassic–Jurassic rifting and Alpine inversion. *Interpretation*, **2**, SM1–SM18.

Salas, R. & Casas, A. 1993. Mesozoic extensional tectonics, stratigraphy and crustal evolution during the Alpine cycle of the eastern Iberian basin. *Tectonophysics*, **228**, 33–55.

Skjerven, J., Rijs, R. & Kalheim, J.E. 1983. Late Paleozoic to early Cenozoic structural development of the south–south eastern Norwegian North Sea. *Geologie en Mijnbouw*, **62**, 35–45.

Soto, R., Casas-Sainz, A.M. & Del Rio, P. 2007. Geometry of half-grabens containing a mid-level viscous decollement. *Basin Research*, **19**, 437–450.

Srivastava, S.P., Roest, W.R., Kovacs, L.C., Oakey, G., Lévesque, S., Verhoef, J. & Macnab, R. 1990. Motion of Iberia since the Late Jurassic: results from detailed aeromagnetic measurements in the Newfoundland Basin. *Tectonophysics*, **184**, 229–260.

Tanveer, M. & Korstgård, J.A. 2009. Structural evolution of the Feda Graben area – A new model. *Marine and Petroleum Geology*, **26**, 990–999.

Taylor, J.C.M. 1998. Upper Permian – Zechstein. *In*: Glennie, K.W. (ed.) *Petroleum Geology of the North Sea*. 4th edn. Blackwell Science, Oxford, 174–211.

Teixell, A., Arboleya, M.L., Julivert, M. & Charroud, M. 2003. Tectonic shortening and topography in the central High Atlas (Morocco). *Tectonics*, **22**, 1051.

Van Wijhe, D.H. 1987. Structural evolution of inverted basins in the Dutch offshore. *Tectonophysics*, **137**, 171–219.

Vendeville, B.C. & Jackson, M.P.A. 1992. The rise and fall of diapirs during thin-skinned extension. *Marine and Petroleum Geology*, **9**, 331–353.

Weijermars, R. 1986. Flow behavior and physical chemistry bouncing putties and related polymers in view of tectonic laboratory applications. *Tectonophysics*, **124**, 325–358.

Withjack, M.O. & Callaway, S. 2000. Active normal faulting beneath a salt layer: an experimental study of deformation patterns in the cover sequence. *AAPG Bulletin*, **84**, 627–651.

Withjack, M.O. & Schlische, R.W. 2006. Geometric and experimental models of extensional fault-bend folds. *In*: Buiter, S.J.H. & Schreurs, G. (eds) *Analogue and Numerical Modelling of Crustal-Scale Processes*. Geological Society, London, Special Publications, **253**, 285–305, http://doi.org/10.1144/GSL.SP.2006.253.01.15

Withjack, M.O., Islam, Q.T. & La Pointe, P.R. 1995. Normal faults and their hanging-wall deformation: an experimental study. *American Association of Petroleum Geologists Bulletin*, **79**, 1–18.

Yamada, Y. & McClay, K.R. 2003*a*. Application of geometric models to inverted listric fault systems in sandbox experiments. Paper 2: insights for possible along strike migration of material during 3D hanging wall deformation. *Journal of Structural Geology*, **25**, 1331–1336.

Yamada, Y. & McClay, K.R. 2003*b*. Application of geometric models to inverted listric fault systems in sandbox experiments. Paper 1: 2D hanging wall deformation an section restoration. *Journal of Structural Geology*, **25**, 1551–1560.

Yamada, Y. & McClay, K.R. 2004. 3-D analog modeling of inversion thrust structures. *In*: McClay, K.R. (ed.) *Thrust Tectonics and Hydrocarbon Systems*. American Association of Petroleum Geologists, Memoirs, **82**, 276–301.

Ziegler, P.A. 1975. Geologic evolution of North Sea and its tectonic framework. *American Association of Petroleum Geologists Bulletin*, **59**, 1073–1097.

Ziegler, P.A. 1982. *Geological Atlas of Western and Central Europe*. Elsevier, Amsterdam.